Master thesis : Study of the vibration compensation with an accelerometer in an Absolute Quantum Gravimeter

Auteur : Verstraeten, Cédric
Promoteur(s) : Collette, Christophe
Faculté : Faculté des Sciences appliquées
Diplôme : Master : ingénieur civil électricien, à finalité spécialisée en "electronic systems and devices"
Année académique : 2022-2023
URI/URL : http://hdl.handle.net/2268.2/17647

University of Liège - Faculty of Applied Sciences

Study of the vibration compensation with an accelerometer in an Absolute Quantum Gravimeter

Master thesis conducted for obtaining the Master's degree of Science in Electrical Engineering major Electronic systems and devices

Supervisor:
COLLETTE Christophe
PhD supervisor:
TELOI Mayana

Author:
VERSTRAETEN Cédric

Academic year 2022 - 2023

Abstract

The Absolute Quantum Gravimeter (AQG) of the French company Exail is a device based on atomic interferometry. It measures local gravity by using cold atoms in free-fall. Unfortunately, vibrations severely degrade the sensitivity and stability of the AQG. This study aims to understand and mitigate vibration-induced noise and improve the performance of the AQG.

A review of the working principle and limitations of the AQG reveals that vibration noise is the primary limiting factor. And among the vibration mitigation techniques analyzed, real-time vibration compensation using additional inertial sensors proves to be the most promising.

Analysis of the gravity signal from the AQG and the signal from the Titan accelerometer highlights the critical role of vibration compensation in achieving sensitive and stable measurements. To understand the vibration compensation mechanism, a thorough evaluation of the relationship between the AQG and the Titan is performed. This evaluation highlights the challenges of correlating vibration and gravitational acceleration. A ground vibration study using seismometers validates the Titan accelerometer measurements and provides insight into the transmissibility of vibrations in the AQG. Finally, post-processing compensation algorithms are tested, but are limited by the low sampling frequency of the AQG, which results in aliasing and non-linear behavior of the vibration transmissibility in the AQG.

Promising avenues for improvement include the evaluation of the IGOR active isolation platform and the µVINS accelerometer to improve AQG performance. Another idea is hybridization with a classical accelerometer to combine AQG stability and accelerometer bandwidth.

In conclusion, this thesis provides valuable insights into the analysis and improvement of AQG performance with a special focus on vibration compensation. The results contribute to a comprehensive understanding of AQG limitations and provide avenues for future advances in gravimetric applications.

Acknowledgements

Contents

List of Figures

Acronyms

µVINS	Compact Vertical Interferometric Inertial Sensor
ADC	Analog to Digital Converter
AQG	Absolute Quantum Gravimeter
ASD	Amplitude Spectral Density
DC	Direct Current
IGOR	Interferometric Gravitational wave ObseRvatory platform
MOT	Magneto-Optical Trap
NHNM	New High Noise Model
NLNM	New Low Noise Model
PML	Precision Mechatronics Laboratory
PSD	Power Spectral Density
QPN	Quantum Projection Noise

Chapter 1

Introduction

1.1 Context

Gravimetry is a field of study that focuses on the temporal and spatial variations of the Earth's gravity, providing insight into the movement of masses beneath the Earth's surface. It finds applications in various fields such as metrology [1], navigation [2, 3], geodesy [4], and geophysics [5].

Absolute gravimeters are instruments used in gravimetry to directly measure the absolute value of the Earth's gravitational acceleration g. Over the years, various types of absolute gravimeters based on different measurement principles have been developed for different applications. In the 1980s, the introduction of absolute gravimeters based on laser interferometry revolutionized gravity measurements, enabling high-precision measurements in the microgal (µGal) range (1 Gal = 0.01 m/s²). The falling corner cube gravimeter became the standard, although its mechanical components imposed limitations. Since the 1990s, gravimeters based on atom interferometry have been investigated as a new measurement method that surpasses the performance of traditional absolute gravimeters [6–8].

In line with this progress, the French company Exail (formerly µQuans) has been working on a cold-atom gravimeter known as the Absolute Quantum Gravimeter (AQG) [8]. In 2016, Exail released the first commercial and portable AQG. An Exail AQG was purchased by the Precision Mechatronics Laboratory (PML) to be studied and to improve its performance.

When comparing absolute gravimeters, certain performance characteristics are considered, the most important of which are sensitivity and long-term stability. Sensitivity refers to the smallest change in gravitational acceleration detectable by the gravimeter and is typically expressed in units of $\mathrm{nm/s^2}/\sqrt{\mathrm{Hz}}$ in gravimetry. Better sensitivity enables the detection of smaller changes in gravity and enhances understanding of Earth's underground behavior and composition. Long-term stability refers to the absence of significant instrument drift over time or correlated noise, typically measured in $\mathrm{nm/s^2}$. In addition to the lack of drift, the long-term stability value represents the precision of the instrument. Other characteristics such as accuracy and repeatability are also important. Accuracy determines the extent to which a gravity measurement can be considered correct in absolute terms, accounting for the uncertainty relative to an absolute standard. And repeatability assesses the agreement between

repeated measurements and is typically evaluated by conducting multiple measurements with changes in location or external parameters. However, the focus is on sensitivity and stability in this work, as they are harder to improve.

Indeed, absolute gravimeters' stability and sensitivity are undermined due to noises. For atom interferometry-based gravimeters, noise is associated with the detection of atoms, as the process is subject to Heisenberg's uncertainty principle. Additionally, electronics, including laser phase, frequency, and intensity, introduce noise. However, the most limiting factor for absolute gravimeters, both atomic and non-atomic, is vibration noise, which has been a significant constraint since their inception [1, 9, 10].

To mitigate the impact of vibrations on AQG measurements, various methods have been developed, including the use of isolation platforms, both passive and active, to cancel vibrations before they reach the gravimeter [11, 12]. Another approach involves using an additional sensor to measure vibrations and subsequently removing them either in real-time during each measurement or in post-processing [8, 13–15]. Exail has implemented a real-time vibration compensation technique using the Titan accelerometer, designed by Nanometrics, to measure vibrations.

Nevertheless, the effectiveness of the technique implemented by Exail has inherent limitations. Since PML acquired the AQG with the aim of improving its sensitivity and stability, a comprehensive understanding of the vibration compensation technique is necessary before any improvements can be made. This research work aims to address this need.

1.2 Overview

To understand the implementation of the vibration compensation technique in an AQG, it is essential to first understand how the AQG itself operates. It is the objective of Chapter 2, which provides an overview of the state-of-the-art atom interferometry principle and its implementation in the AQG. Once the fundamental working principles of the AQG have been established, a study of its limitations offers insights into the different noise sources that impact its performance. Typical noise values provided by Exail are presented, and the intrinsic limitations of the AQG's working principle are briefly described. Vibrational noise, which surpasses other noise sources, is further analyzed, and its theoretical impact on the AQG is presented through the formalism of the sensitivity function developed by G. John Dick for the atomic clock. Existing vibration mitigation techniques, such as vibration isolation and vibration compensation, are presented and compared.

After establishing the state-of-the-art, Chapter 3 delves deeper into the analysis of vibration compensation with Titan to understand its implementation and explore possibilities for improvement. First, a comprehensive analysis of a typical gravity signal output by the AQG after its processing through MATLAB is presented. The time series, Power Spectral Density (PSD), and Allan deviation of the gravitational signal are analyzed. Once the compensated gravity signal is understood, the value added by Titan is examined starting with an understanding of the sensor itself, its usage, and its limitations. It is crucial for comprehending the signal processing implemented by Exail in the acquisition of the Titan signal, which is presented and discussed afterwards. The analysis then focuses on

the signals obtained from the uncompensated AQG and from the Titan, as well as their correlation. The analysis is performed in acceleration to determine whether a simple intuitive relationship exists or not. To validate the analyzed signal from Titan, a complementary study is conducted using two seismometers. The study also provides insights into the transmissibility of ground vibrations into the AQG. Finally, attempts at developing a post-processing vibration compensation algorithm are presented and discussed.

Following the detailed analysis of Titan compensation, Chapter 4 delves into the prospects for improving the current technology. First, the use of an active isolation platform in PML to further reduce vibration noise, in addition to vibration compensation, is discussed. Preliminary results are presented. Secondly, the use of a Compact Vertical Interferometric Inertial Sensor, the μVINS, is explored, as it has the potential to offer improved vibration compensation. However, further investigation is required in this regard. The final potential improvement presented is the hybridization of the AQG with a classical accelerometer. This final part is a theoretical review that builds upon previous work and presents a revolutionary approach to AQG measurements, combining the stability and sensitivity of the AQG with the broad bandwidth of a classical accelerometer.

Finally, the conclusion of this thesis presents a summary of the work done with the key findings and outlines avenues for future improvement.

Chapter 2

What is an Absolute Quantum Gravimeter ?

The Absolute Quantum Gravimeter (AQG) is an absolute gravimeter that uses the principles of laser interferometry and the wave-like properties of cold atoms to measure the absolute local gravity. This chapter provides an overview of Exail's AQG composition, followed by an analysis of its measurement principle and the underlying physics. The limitations of the AQG are discussed, including various noise sources that affect measurements, as well as the constraints imposed by the AQG's working principle. The vibration noise that emerges as the most problematic is examined in detail and potential techniques for its mitigation are presented, focusing on vibration isolation and vibration compensation.

2.1   AQG composition

The AQG consists of two main components: the sensor head and the control unit. The sensor head, as illustrated in Figure 2.1, houses the vacuum chamber where the cold atoms are subjected to free-fall and participate in the interferometric process enhanced by laser pulses [8].
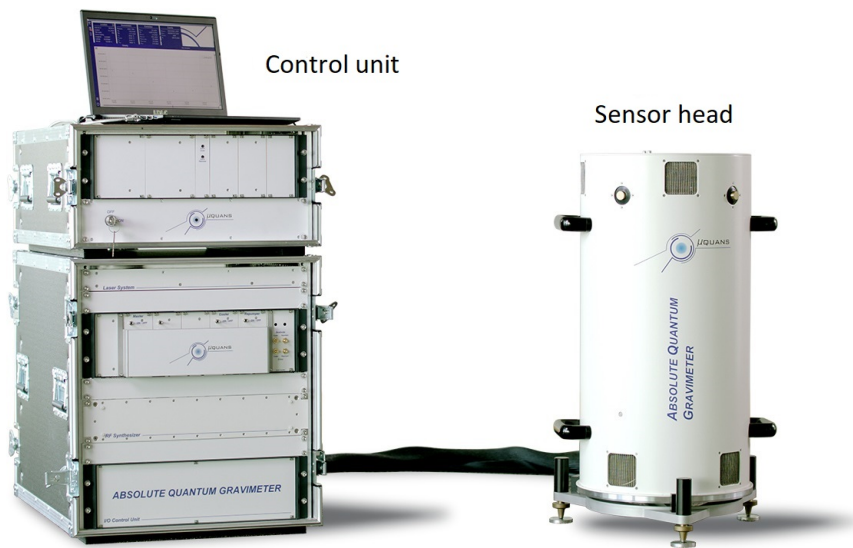
Figure 2.1. Absolute Quantum Gravimeter composition. Adapted figure from [8].

A Magneto-Optical Trap (MOT) is placed at the top of the vacuum chamber. It comprises two coils that generate the magnetic field required for trapping the atoms, along with three pairs of counter-propagating lasers responsible for cooling the atoms to a few μK, effectively reducing their kinetic energy [16]. The MOT is the initial location for the atoms before they are released into free-fall. Figure 2.2 shows a conceptual scheme of the MOT.
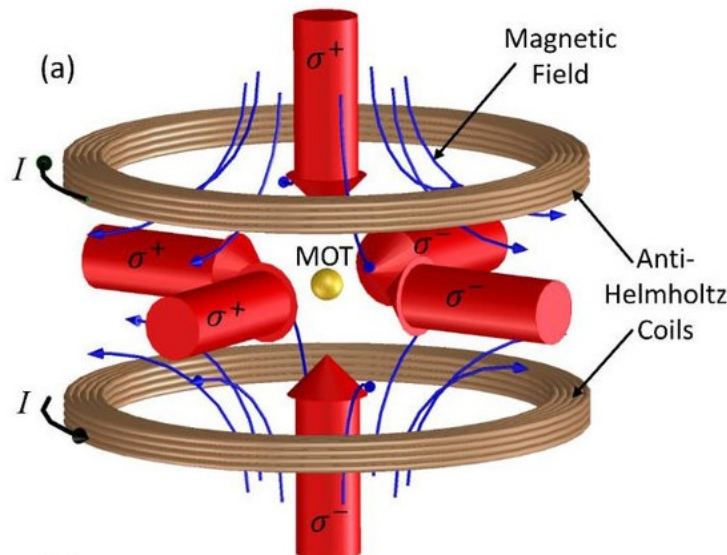
Figure 2.2. MOT design. Figure from [16].

The MOT uses a pyramid reflector as depicted in Figure 2.3 , reducing the need for multiple lasers. Due to the shape of the pyramid reflector, only two laser beams are needed as they are reflected in different directions, mimicking the effect of multiple beams. Therefore the presented design simplifies the cooling process as only two laser beams are required instead of six. Furthermore, these two laser beams are also used throughout the rest of the process.

The sensor head also includes various sensors such as a pressure gauge, tiltmeters, temperature sensors, a GPS receiver, and a 3D accelerometer, enabling various parameters to be monitored [17]. The accelerometer plays a crucial role in this research work as it is used in the vibration compensation mechanism.
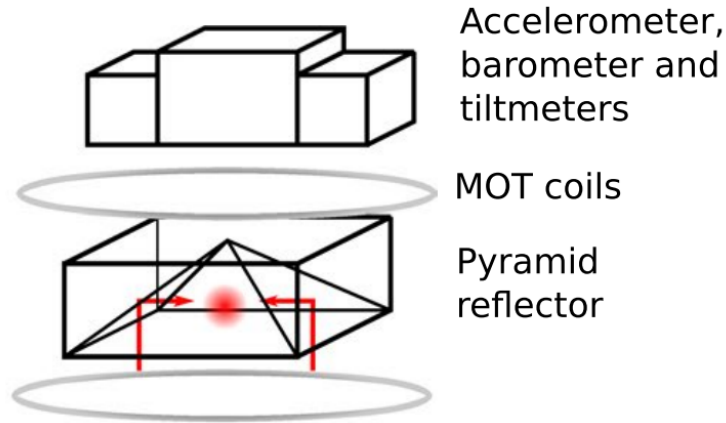
Figure 2.3. Pyramidal reflector in the MOT and sensors used on top. Figure from [8].

The control unit encompasses the software responsible for automating the operations of the AQG. It processes the acquired data in real-time and performs calibration adjustments when necessary. Additionally, the control unit manages the laser system which consists of one master reference laser emitting at 1560 nm, and frequency-doubled, and two slave lasers used for cooling, pumping, and Raman excitations of the atoms. The two slave lasers are frequency offset-locked to the master laser [8, 18].

2.2   Measurement principle

The measurement cycle of the AQG consists of three main stages: atoms trapping and cooling, interferometer, and detection. The first stage essentially involves preparing the atoms in the MOT before dropping them. Then the interferometer consists of the free-fall of the atoms and the use of lasers to change their state. Finally, the detection analyzes the different states taken by the atoms and deduces the absolute gravity based on that. These three stages are depicted in Figure 2.4a, where the start of the free-fall is considered as a part of the trapping and cooling stage. They are explained in detail below. Figure 2.4b shows the times associated with each one of the stages. The total duration of a measurement cycle is 540 ms.
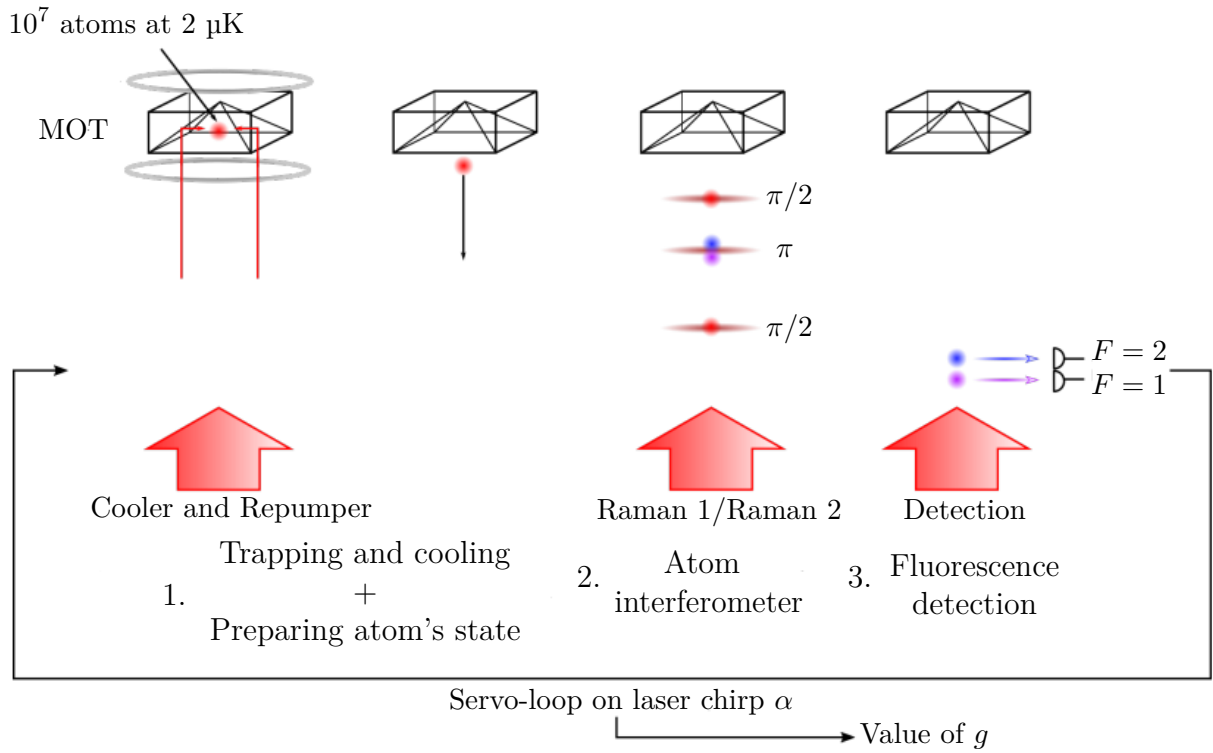
(a) Simplified stages. Adapted Figure from [8].
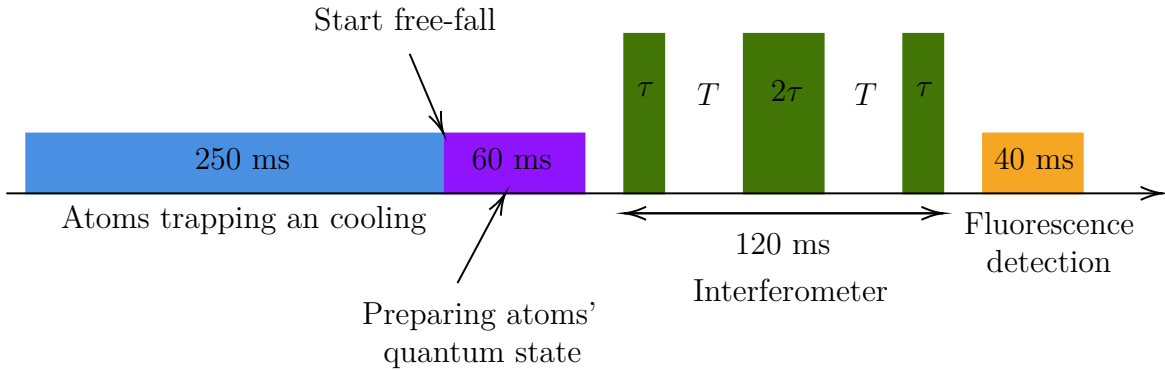
(b) Timeline, with $\tau = 7$ µs and $T = 60$ ms. The total duration of a cycle is 540 ms.

Figure 2.4. Measurement cycle of an AQG.

Atoms trapping and cooling

A cloud of approximately 10^7 ^{87}Rb atoms is loaded into the MOT and laser-cooled to temperatures below 2 µK to reduce their velocities and prevent collisions. The cooling process results in a denser cloud and atoms with reduced kinetic energy, minimizing the ballistic expansion of the cloud during free-fall and preventing the atoms from hitting the walls. The effect of temperature on the cloud expansion is illustrated in Figure 2.5. For a temperature of 2 µK, the cloud expands by only 30 µm in diameter every 1 ms, which is approximately 15000 times smaller compared to the expansion at 300 K.

The term "cold atoms" is used when atoms are cooled to a temperature where their behavior is governed by quantum mechanics rather than classical mechanics. At such low temperatures, atoms can no longer be described as distinct particles with well-defined positions and velocities. Instead, each atom behaves like a wavepacket[1]. The center of the wavepacket moves and evolves over time, but it still obeys the laws of classical mechanics, so it will follow a free-fall trajectory under the influence of gravity [8, 16].

300 K

0.5 m/ms expansion

$T°$

2 µK

30 µm/ms expansion

Figure 2.5. Effect of temperature on an atom cloud ballistic expansion.

Once the cooling process is finished, the MOT coils and lasers are switched off, which causes the atoms to fall freely. Just before entering the interferometry stage, a selection process is performed to isolate atoms in the state $|5^2S_{1/2}, F = 1, m_F = 0\rangle$ while removing atoms in other states. The selection is achieved using a microwave pulse [8, 10, 16].

Interferometer

The atomic interferometer for absolute gravimeters follows a Mach-Zehnder-like geometry, which involves separating the atoms into two groups, manipulating their states, and subsequently recombining them. This process relies on the use of Raman pulses that induce Raman transitions in the atoms as a function of the pulses properties.

---

[1]A wavepacket behaves like a wave in that it undergoes interference and diffraction, but like a particle in that it has a definite position and momentum.

According to R. Geiger *et al.*[19], "During a Raman transition, the atom interacts with two counter-propagating lasers of angular frequencies ω_1 and ω_2 and wavevectors k_1 and k_2. These two light fields are detuned [in frequency by Δ] from a strong electronic transition but their frequency difference matches the energy difference between two fundamental atomic states $|a\rangle$ and $|b\rangle$, which are then coupled by the light fields in a so-called lambda scheme (Figure 2.6). Atoms initially in the state $|a\rangle$ will absorb a photon in the laser 1 and de-excite by stimulated emission of a photon in the laser 2, ending up in the state $|b\rangle$. Conservation of momentum implies that the two coupled states differ in momentum by the momentum transfer $\hbar\left(\vec{k_1} - \vec{k_2}\right) = \hbar\vec{k}_{\text{eff}}$ ($k_{\text{eff}} = |\vec{k_1}| + |\vec{k_2}|$ for counter-propagating beams)."
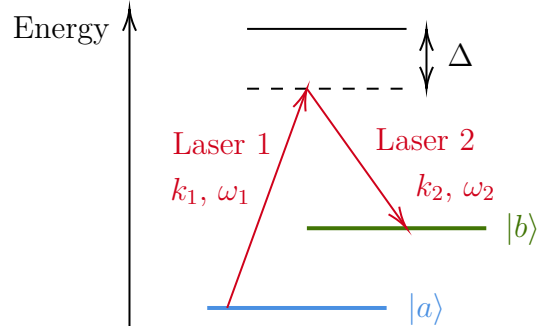
Figure 2.6. Raman transition in an atom.

In this extract, $\vec{k}_{\text{eff}} = \vec{k_1} - \vec{k_2}$ is the effective wavevector and $k_{\text{eff}} = |\vec{k_1}| + |\vec{k_2}|$ is its amplitude. $\hbar = h/2\pi$, where $h = 6.62607015 \times 10^{-34}$ J·s is the Planck's constant.

In the case of gravimetric measurements, the two hyperfine levels of the ground state $5^2S_{1/2}$ in ^{87}Rb atoms are used: the fundamental level $|5^2S_{1/2}, F = 1, m_F = 0\rangle$, and the excited level $|5^2S_{1/2}, F = 2, m_F = 0\rangle$. These two levels correspond respectively to $|a\rangle$ and $|b\rangle$ in Figure 2.6. To realize the atomic interferometer, the atomic cloud experiences three Raman pulses during its free-fall. The pulse configuration commonly used for gravimetric measurements is $\pi/2 - \pi - \pi/2$ [8], with durations of $\tau - 2\tau - \tau$, respectively. In the case of the AQG, the pulse duration $\tau = 7$ μs, and the interrogation time between each pulse $T = 60$ ms, are used.

The Raman pulses can be associated with the components of an optical Mach-Zehnder interferometer [19]. The atomic interferometer consists of the following steps:

1. The first pulse, $\pi/2$, acts as a beamsplitter, dividing the cloud of atoms in two. It has a transition probability in the internal atom states of 50%. As a result, half of the atoms end up in the state $|F = 1\rangle^2$, while the other half end up in the state $|F = 2\rangle$. The atoms in state $|\text{F} = 2\rangle$ experience a change in momentum, resulting in a net deceleration or acceleration of the atoms by a quantity of $\hbar\vec{k}_{\text{eff}}/M$ (where M is the mass of the atoms) depending on the direction of the lasers, as shown in Figure 2.7. In the AQG, the design is such that it slows down the fall of the atoms [8].
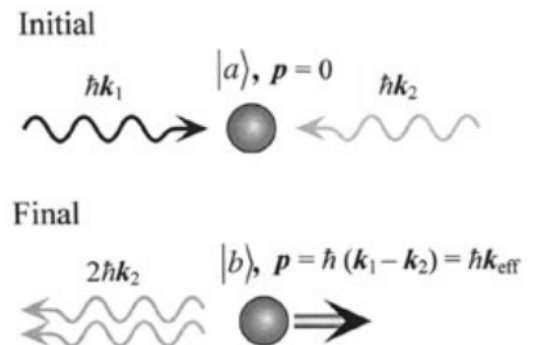
Figure 2.7. Change in the atom's momentum after a Raman transition. Figure from [9].

2. The second pulse, π, acts as a mirror, swapping the states of the two atom groups. It has a transition probability in the atom's internal states of 100% [19].

3. Finally, the last pulse, $\pi/2$, acts as another beamsplitter. It probabilistically changes 50% of the atoms in the state $|F = 1\rangle$ (where the atoms in the cloud are with 50% probability) into the excited state $|F = 2\rangle$, and vice versa. At the output of the interferometer, some atoms end up in state $|F = 1\rangle$, others in state $|F = 2\rangle$. The proportion of atoms in each one of these states is used to measure gravity [19].
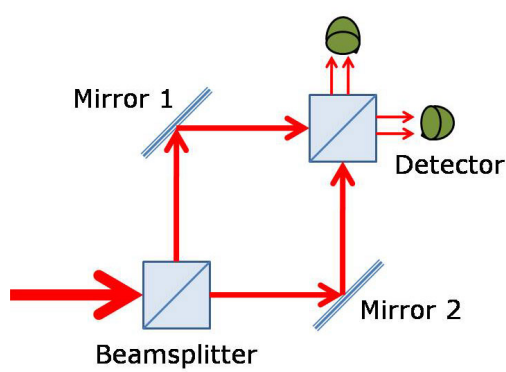
(a) Optical Mach-Zehnder interferometer.
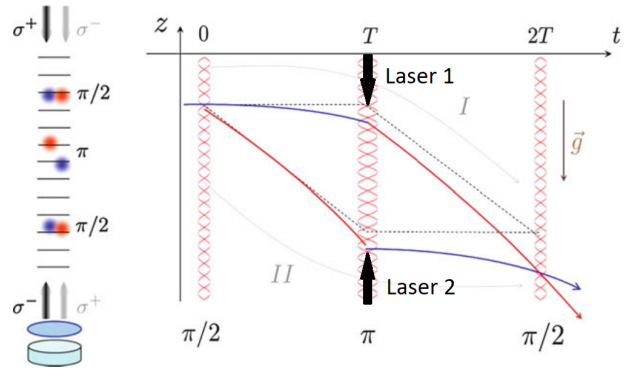
(b) Atomic Mach-Zehnder interferometer. Adapted figure from [18].

Figure 2.8. Parallel between an optical and an atomic Mach-Zehnder interferometer.

Figure 2.8b illustrates the vertical displacement of the atoms as a function of time. The dotted black lines indicate the trajectory the atoms would follow in the absence of gravity. However, due to the presence of gravity, the atoms exhibit an increased velocity as the free-fall progresses. It can be seen with the blue and red curves. As previously explained, the atoms in the state $|F = 2\rangle$ fall slower due to their reduced momentum, thus the blue lines in Figure 2.8b correspond to atoms in the excited state, while the red ones represent the trajectory of the atoms in the fundamental state.

Throughout the free-fall, atoms accumulate phase changes with each light pulse. A pulse induces a change in the atomic state, along with a shift in the atomic wavefunction phase. The phase shift effect is further explained in the detection stage.

Detection

The final measurement step is to determine the proportion of atoms in each of the two states [8, 10, 15, 18, 19]. It is achieved through state-selective fluorescence detection at the bottom of the chamber, where the number of atoms in each level is counted, and the interference pattern and corresponding interferometric phase shift are measured. The transition probability P, i.e. the probability that an atom changes its state, is given by $P = \frac{C_e}{C_f + C_e}$, where C_f (resp. C_e)

---

[2]In the following the notation $|F = 1\rangle$ (resp. $|F = 2\rangle$) instead of $|5S_{1/2}, F = 1, m_F = 0\rangle$ (resp. $|5S_{1/2}, F = 2, m_F = 0\rangle$) will be used for the state of the atoms in order to not surcharge the text and the equations.

represents the proportion of atoms in the fundamental state (resp. excited state). Therefore, P also represents the proportion of atoms in state $|F = 2\rangle$ at the end of the interferometer. If all atoms end up in the excited state, P equals 1; if they all end up in the fundamental state, P is 0; and it lies between 0 and 1 for a mixture of states.

The transition probability can be related to the formula of a classical two-wave interferometer as follows [8]:

$$P = P_0 - \frac{C}{2} \cos \Delta\phi \tag{2.1}$$

Here, P_0 is the average transition probability, ideally equal to 0.5, and $C = \frac{P_{max} - P_{min}}{P_{max} + P_{min}}$ is the contrast. Its ideal value is 1 ($C \approx 0.4$ for the AQG [8]). Higher contrast is desirable as it makes the interference fringes more visible. The relationship between P and $\Delta\phi$ is visible in Figure 2.9.
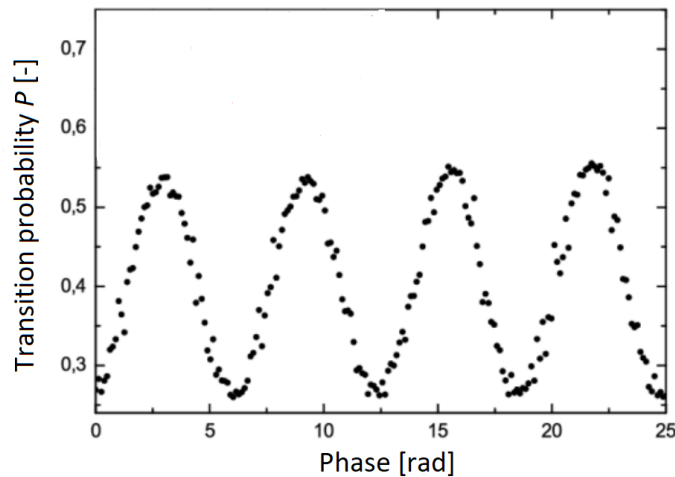
Figure 2.9. Typical measurement of the transition probability as a function of the interferometric phase. Adapted Figure from [16].

In Equation 2.1, $\Delta\phi$ represents the interferometric phase shift. It is induced by the phase shift applied to the atomic wavefunction at each light pulse. When a change in the state of the atoms occurs, a slight phase shift of

$$\phi = \frac{4\pi}{\lambda} x(t) - (\omega_1 - \omega_2)t = k_{\text{eff}} x(t) - \omega_{\text{eff}} t \tag{2.2}$$

is experienced by the atomic wavefunction [9]. Here, $k_{\text{eff}} = k_1 + k_2 = 4\pi/\lambda$ represents the amplitude of the effective wavevector, $\lambda = 780$ nm is the wavelength of the lasers, $x(t)$ is the vertical position of the atom's center of mass at the moment of the pulse compared to its position at the first pulse, $\omega_{\text{eff}} = \omega_1 - \omega_2$ is the effective frequency, and t is the time elapsed since the first pulse [8]. The interferometric phase $\Delta\phi$ is then defined as the difference between the phase shift ϕ_U accumulated by the atoms following the upper path in Figure 2.8b and the phase shift ϕ_L accumulated by those following the lower path, giving $\Delta\phi = \phi_U - \phi_L$ [9, 16].

The atoms in the upper path experience two phase shifts: a positive one at the first light pulse at $t = 0$ and a negative one at the second pulse at $t = T$. Thus, $\phi_U = k_{\text{eff}} x(0) - (k_{\text{eff}} x(T) - \omega_{\text{eff}} T) = \phi_1 - \phi_2$.

Similarly, the atoms in the lower path also experience two phase shifts: a positive one at the second pulse and a negative one at the last pulse. Hence, $\phi_L = (k_{\text{eff}}x(T) - \omega_{\text{eff}}T) - (k_{\text{eff}}x(2T) - \omega_{\text{eff}}2T) = \phi_2 - \phi_3$.

Taking the final difference:

$$\begin{aligned} \Delta\phi &= \phi_U - \phi_L \\ &= k_{\text{eff}}\left(x(0) - 2x(T) + x(2T)\right) \\ &= \phi_1 - 2\phi_2 + \phi_3 \end{aligned} \tag{2.3}$$

The terms involving ω_{eff} cancel each other out.
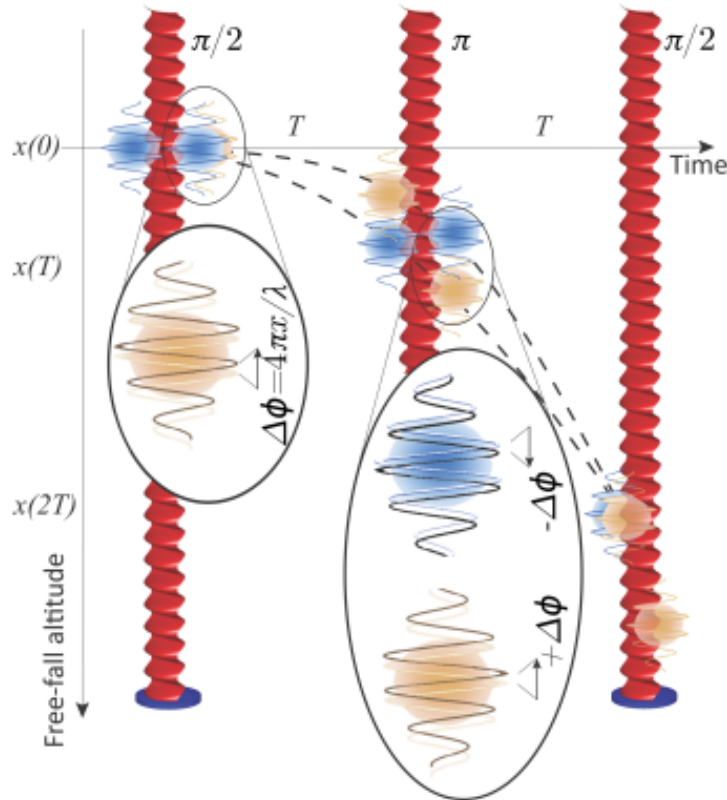
Figure 2.10. Phase shifts induced by the Raman transitions during the free-fall of the atoms. Figure from [8].

Figure 2.10 gives a visual representation of the phase shifts experienced by the atoms.

Since the position can be related to acceleration using the simple mechanic's formula $x(t) = x_0 + vt + \frac{1}{2}at^2$, it gives:

$$\begin{aligned} \Delta\phi &= k_{\text{eff}}\left(x(0) - 2x(T) + x(2T)\right) \\ &= k_{\text{eff}}\left(-2\frac{1}{2}gT^2 + \frac{1}{2}g(2T)^2\right) \\ &= k_{\text{eff}}gT^2 \end{aligned} \tag{2.4}$$

It is evident that in the absence of gravity, $\Delta\phi$ would be equal to 0. However, since gravity affects the system, it is not the case. Furthermore, as the atoms are in free-fall, the Doppler

effect in the lasers must be taken into account. It introduces an additional phase shift due to the difference in frequencies perceived by the atoms from the top and bottom lasers. Since this effect varies for each of the three pulses, it is compensated by applying an adjustable chirp signal α [Hz/s] to the frequency difference between the two lasers. Consequently, the effect of the chirp on the interferometric phase is [8, 9, 20, 21]:

$$\Delta\phi = (k_{\text{eff}}g - 2\pi\alpha)T^2 \tag{2.5}$$

The chirp α is advantageously exploited and is tuned such that $\Delta\phi = 0$. During the initial calibration at the start of the AQG, the chirp is locked to a value that nullifies the interferometric phase. Subsequently, a servo-loop maintains the chirp around this value to keep the interferometric phase at zero. As gravity varies with time, α needs to be updated at each cycle.

By having an interferometric phase set to zero, g can be easily determined by using the previous equation:

$$\begin{aligned} \Delta\phi &= (k_{\text{eff}}g - 2\pi\alpha)T^2 = 0 \\ \Longleftrightarrow g &= \frac{2\pi\alpha}{k_{\text{eff}}} \end{aligned} \tag{2.6}$$

However, various noise sources introduce an additional phase variation $\delta\varphi$, which affects the interferometric phase and consequently the performance of the gravimetric measurement. The limitations due to such effects are explained in the next section.

2.3   Limitations

Like any sensor, the AQG is subjected to various constraints, such as noise and limitations associated with its working principle. Gravimetric measurements in the AQG are affected by different types of noise, e.g. electronic noise, Quantum Projection Noise (QPN), laser noise, and so on. Although many noise sources are effectively mitigated, it is important to discuss the most important ones. There are three categories of noise in the AQG: detection noise, laser phase noise, and vibration noise. These three categories are detailed in Section 2.3.1.

Limitations due to the sequential measurement cycle and thus the low sampling rate of the AQG exist as well. They are discussed in Section 2.3.2.

Lastly, some systematic effects are presented is Section 2.3.3. They are not considered as random noise but rather as predictable biases. They must be compensated for, otherwise they would undermine the AQG performances.

2.3.1   Noises

As introduced, noises in an AQG can be classified into three main groups. The first one, the detection noise, affects directly the transition probability P of the interferometer. Since the

transition probability is used to determine the interferometric phase and thereby the gravity, it has an impact on the output signal.

On the other hand, laser phase noise and vibration noise affect the interferometric phase in the AQG by introducing an additional phase factor denoted as $\delta\varphi = \delta\varphi_{\text{laser}} + \delta\varphi_{\text{vib}}$ [14, 22–26]. Consequently, the interferometric phase can be expressed as follows :

$$\Delta\phi = (k_{\text{eff}}g - 2\pi\alpha)T^2 + \delta\varphi \tag{2.7}$$

To assess the impact of the different noises affecting the sensitivity of the instrument, it is important to evaluate their standard deviation σ. It provides an indication of the measurement fluctuations. In order to compare and analyze the effects on both, the interferometric phase (σ_ϕ) and the gravitational acceleration (σ_g), Equation 2.4 can be used. As a result:

$$\sigma_\phi = k_{\text{eff}}\sigma_g T^2 \tag{2.8}$$

The numerical values referenced in the following sections to quantify the noises were provided by Exail, the company that developed the AQG. The given values are the results of numerous tests ran by Exail, where the amplitude of the effective wavevector was assumed to be $k_{\text{eff}} = 16 \times 10^6$ [27].

Detection noise

Detection noise is generally divided into three groups: (1) technical noise such as shot noise in electronics, (2) the Quantum Projection Noise (QPN), and (3) optical noise due to laser frequency and intensity fluctuations [9, 15, 16, 24, 28].

The QPN represents the fundamental limit imposed by the uncertainty principle of quantum mechanics, which states that it is impossible to simultaneously know the precise position and velocity of a particle, such as a photon or an electron. In the AQG, when measuring the phase of the atom interferometer, the atoms are detected using a fluorescence detection scheme. The number of photons detected during the detection is proportional to the number of atoms in a specific energy level. However, due to the uncertainty principle of quantum mechanics, it is impossible to prepare the atoms in a pure energy state, leading to fluctuations in the number of photons detected in each measurement. The resulting uncertainty sets a limit to the resolution, and the standard deviation of the transition probability due to the QPN is given by $\sigma_P = \sqrt{\frac{P(1-P)}{N}} = 1/2\sqrt{N}$ when operating at the mid-fringe point ($P = 0.5$), where N is the number of atoms detected [15, 24].

However, the QPN limit is never reached in practice, as other noises will surpass it. Typically in the detection noise, the technical and optical noises have a higher level than the QPN.

According to the information provided by Exail, the standard deviation of the transition probability due to detection noise, σ_P, is approximately 10^{-3} shot^{-1} for the AQG. It converts into phase noise, as $\sigma_\phi = 0.4$ mrad/shot. And into gravitational noise it gives 7 nm/s^2/shot. The unit "per shot" gives the deviation on one measurement, when averaged it is lowered.

Laser phase noise

Laser phase noise is a significant factor limiting the sensitivity of the AQG. It introduces uncertainty into the Raman lasers' phase and therefore into the atomic interference fringe pattern, affecting the sensitivity of gravity measurements. There are three main sources of the laser phase noise [9, 11, 15, 19].

- **Phase-lock loop noise**: The phase-lock loop is used in the AQG to stabilize the lasers' phase. However, the process is not perfect and can introduce noise into the phase of the lasers.

- **Microwave frequency source noise**: The microwave frequency source generates the Raman lasers' frequency in the AQG. If it is noisy, it can induce phase fluctuations in the Raman lasers.

- **High-frequency phase noise**: The process of increasing the lasers' frequency up to the right one also increases the white noise of the lasers' phase. It, therefore, amplifies the uncorrelated phase fluctuations in each of the interferometer pulses.

Although Exail has made efforts to mitigate the phase noise during the development of the AQG, it is inherent to the instrument and can only be reduced to a certain extent by optimizing the electronic and laser components. The laser phase noise contributes to the AQG's self-noise, and its reduction requires tackling the underlying noise sources directly.

According to Exail's tests, laser phase noise in the AQG amounts to $\sigma_{\phi,\text{laser}} = 20$ mrad/shot, resulting in an influence of 350 nm/s^2/shot on g.

Vibration noise

Vibration noise, induced by ground vibrations, represents the most significant noise source in the AQG.

Since most of the optical components of an AQG experience vibration noise in common-mode, the primary impact is on the reflective mirror (the pyramidal reflector has the same role as a flat reflective mirror during the Raman pulses) placed at the top of the vacuum chamber. The mirror, used for Raman lasers, can have its position altered by vibrations. Consequently, the phase of the reflected beam is altered by the change of position of the mirror, as represented in Figure 2.11, and the interferometric phase $\Delta\phi$ at the output as well. Indeed, the phase modifications ϕ_1, ϕ_2 and ϕ_3 applied to the wavepackets during their fall, via the Raman transition, are altered [10, 14].
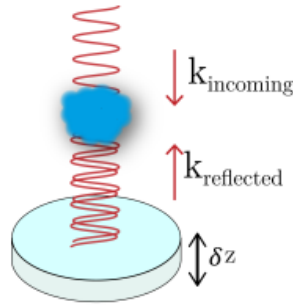
Figure 2.11. Phase noise induced by the mirror vibrations. Figure from [14]

If the mirror undergoes a vertical vibratory displacement $\delta_z(t)$, the phase noise introduced by the Raman light due to vibrations is given by $k_{\text{eff}}\delta_z(t)$ [10].

The effect on the interferometric phase is derived from Equation 2.7 and gives:

$$\Delta\phi = \phi_1 - 2\phi_2 + \phi_3 + k_{\text{eff}}\delta_z(t) \tag{2.9}$$

Vibration noise is the focus of this research work, along with numerous others such as B. Fang *et al.* [1], V. Ménoret *et al.* [8], A. Peters *et al.* [9], R. Geiger *et al.* [19], to give some examples. It represents the most significant noise source and demands attention since the highest noise level sets the sensitivity limits.

Exail conducted tests and achieved a vibration noise level of around $\sigma_{\phi,\text{vib}} = 50$ mrad/shot, which corresponds to 870 nm/s²/shot after vibration compensation in Talence, France. In a seismically quieter site such as Larzac, France, they almost reached the self-noise limit of the AQG with 450 nm/s²/shot [27]. Due to the volatility of vibration noise without vibration isolation, the actual noise levels can vary considerably depending on the location and time of day.

In summary, QPN represents the intrinsic limit of the AQG's sensitivity. Laser phase noise constitutes the self-noise of the instrument and can only be reduced by modifying the electronic and laser components themselves. Vibration noise, the most significant noise source, affects the laser phase through the displacement of the reflective mirror and will be further discussed in Section 2.4, along with potential mitigation techniques.

The summary of the noise sources is presented in Table 2.1.

Noise	Source	σ_ϕ [mrad/shot]	σ_g [nm/s²/shot]
QPN	Intrinsic limit due to the uncertainty in atom detection (Heisenberg's principle)	0.4	7
Laser phase	Self-noise in the AQG due to phase fluctuations from various effects	20	350
Vibration	Highest noise source arising from ground vibrations	Depends on location	Depends on location

Table 2.1. Summary of noise sources.

2.3.2 Deadtime limitations

The working principle of the AQG introduces certain limitations that need to be considered. Firstly, the AQG operates sequentially, where a measurement cycle begins once the previous one has been completed. Consequently, the deadtime between each measurement reduces the sampling rate of the AQG, approximately $f_c = 1/T_c \simeq 2$ Hz in our case [29]. The low sampling rate arises due to the time required to prepare the atoms in the MOT and the duration of the interrogation time $2T$. Thus, a compromise must therefore be made. Reducing the preparation time reduces the number of atoms available for the measurement, leading to reduced precision. Similarly, shortening the interrogation time allows for a faster sampling rate but sacrifices the measurement's precision as Equation 2.4 shows. A shorter T means less contrast in the interferometric pattern. Therefore, a tradeoff between sampling rate and instrument performances exists.

In addition to the low sampling rate, the AQG exhibits a limited dynamic range. The interferometric phase $\Delta\phi$ depends on the acceleration g, as described by Equation 2.4. However, in the detection process (Equation 2.1), the phase appears within a cosine function. Consequently, different accelerations can produce the same transition probability P, which is then used to determine the interferometric phase. To address this issue, Exail uses a chirp α to keep the phase close to zero, ensuring that the AQG operates around the central fringe of the interferometric pattern [8]. This strategy is crucial because a difference in the interferometric phase of $\pm\pi$ becomes indistinguishable. Furthermore, vibrations pose a significant challenge since they can introduce a phase shift larger than π, effectively disrupting the interferometric pattern.

2.3.3 Systematic effects

Systematic effects include all the disturbances that induce a bias but are predictable. Through the use of additional sensors or simply known physical phenomenons, the systematic effects

are fully compensated in the measurement [9]. The following non-exhaustive list briefly summarizes some of them in order to understand their origin and cause:

- **Coriolis effect**: The Earth's rotation causes the Coriolis effect. As the AQG is sensitive to the direction of gravity, any rotation of the system results in a phase shift of the interferometer output.

- **Wavefront aberration**: Imperfections in the optics used to manipulate and probe the atoms can lead to wavefront aberration. It results in variations in the intensity and phase of the laser beams, affecting the trajectories of the atoms and their interference patterns.

- **Two-photon light effect**: It arises from the interference between the two paths of the atom interferometer. When two atoms pass simultaneously through the Raman pulses, they can emit or absorb two photons simultaneously, creating a source of variation known as two-photon light. This effect scatters photons in random directions and alters the interference pattern of the atoms, reducing the measurement sensitivity.

- **Magnetic field gradients effect**: Spatial variations in the magnetic field can lead to differences in the energy levels of the atoms through the Zeeman effect, affecting the interferometer phase.

- **One-photon light shift effect**: The interaction between the laser beam and the atoms in the interferometer can cause a one-photon light shift. This interaction shifts the energy levels of the atoms, leading to a phase shift in the interferometer.

- **Refractive index of background vapor effect**: The interaction of the atoms, during the interferometer, with the surrounding vapor, which has a fluctuating refractive index, induces variations in the phase of the laser light used to manipulate the atoms. This, in turn, introduces a variation in the phase of the laser in the AQG. The magnitude of this variation depends on the variation in the refractive index of the surrounding vapor and the interaction time between the atoms and the vapor.

The overall bias due to the systematic effects is estimated at -108.89 nm/s^2. Therefore, a correction of 108.89 nm/s^2 is automatically applied at each measurement to compensate for it [30].

2.4   Vibration mitigation techniques

To assess the impact of vibrations on the AQG, it is essential to examine the behavior of signals in the frequency domain. In doing so, it is necessary to analyze the transfer function of the reflective mirror's sensitivity to vibration noise, as it provides insights into how vibrations affect the AQG [10].

The sensitivity transfer function of the AQG has been extensively studied in the Ph.D. thesis of P. Cheinet [24] and A. Landragin [25]. These studies use a powerful tool known as the

sensitivity function, which characterizes the effect of a small disturbance in the laser phase on the transition probability P. Through mathematical development, they extend its application to describe the effect of such a disturbance on the interferometric phase. Furthermore, they demonstrate how a small disturbance in acceleration affects the transition probability and, consequently, the interferometric phase. This formalism is based on the work of G. John Dick on atomic clocks. The sensitivity function takes the following shape and expression to describe the effect of vibration in the AQG [14]:

$$
f(t) = \begin{cases}
\frac{2}{\Omega_R}\left(1 - \cos\left(\frac{\Omega_R}{2}t\right)\right) & \text{if} \quad 0 < t \leq \tau \\[2mm]
t + \frac{2}{\Omega_R} - \tau & \text{if} \quad \tau < t \leq \tau + T \\[2mm]
T + \frac{2}{\Omega_R}\left(1 - \cos\left(\frac{\Omega_R}{2}(t - T)\right)\right) & \text{if} \quad \tau + T < t \leq 3\tau + T \\[2mm]
2T + \frac{2}{\Omega_R} + 3\tau - t & \text{if} \quad 3\tau + T < t \leq 3\tau + 2T \\[2mm]
\frac{2}{\Omega_R}\left(1 - \cos\left(\frac{\Omega_R}{2}(t - 2T)\right)\right) & \text{if} \quad 3\tau + 2T < t \leq 4\tau + 2T \\[2mm]
0 & \text{Otherwise.}
\end{cases} \tag{2.10}
$$
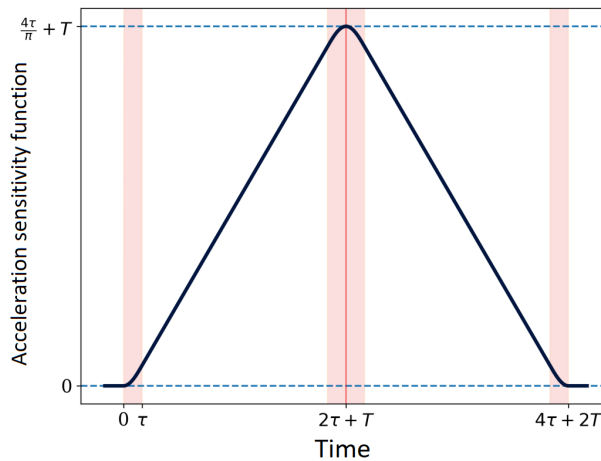
Figure 2.12. Acceleration sensitivity function $f(t)$ of the AQG. Adapted Figure from [14]

The function presented in Figure 2.12 is the sensitivity function when working with acceleration disturbances. The shape of the sensitivity function for laser phase disturbances is different but irrelevant in the context of this work.

Using the Fourier transform, the sensitivity function can be analyzed in the frequency domain, leading to the expression of the sensitivity transfer function $H_a(\omega)$ that characterizes the effect of acceleration disturbances on the interferometric phase across the entire frequency spectrum, with $\omega = 2\pi f$. Similarly, the transfer function $H_\phi(\omega)$ describes the relationship between a disturbance in the laser phase and $\Delta\phi$.

In this work, the sensitivity transfer function $H_a(\omega)$ is focused because vibrations are the primary noise of interest, and they are usually treated in terms of accelerations.

By applying this formalism, the following relationship is derived [24, 25]:

$$H_a(\omega) = \frac{k_{\text{eff}}}{\omega} \frac{4\Omega_R}{\omega^2 - \Omega_R^2} \sin\left(\frac{\omega(T+2\tau)}{2}\right) \left(\cos\left(\frac{\omega(T+2\tau)}{2}\right) + \frac{\Omega_R}{\omega} \sin\left(\frac{\omega T}{2}\right)\right) \quad (2.11)$$

Here, T represents the interrogation time between two Raman pulses, τ denotes the pulse duration, and $\Omega_R = \pi/2\tau$ corresponds to the Rabi frequency[3].

Nonetheless, in many cases, this expression can be simplified. When $\tau << T$ and $\omega << \Omega_R$, which is typically the case in the AQG, the expression can be approximated as follows:

$$\begin{aligned} H_a(\omega) &= \frac{k_{\text{eff}}}{\omega} \frac{4\Omega_R}{\omega^2 - \Omega_R^2} \sin\left(\frac{\omega(T+2\tau)}{2}\right) \left(\cos\left(\frac{\omega(T+2\tau)}{2}\right) + \frac{\Omega_R}{\omega} \sin\left(\frac{\omega T}{2}\right)\right) \\ &\simeq \frac{-4k_{\text{eff}}}{\omega\Omega_R} \sin\left(\frac{\omega T}{2}\right) \left(\frac{\Omega_R}{\omega} \sin\left(\frac{\omega T}{2}\right)\right) \\ &= \frac{-4k_{\text{eff}}}{\omega^2} \sin^2\left(\frac{\omega T}{2}\right) \\ &= -k_{\text{eff}} T^2 \operatorname{sinc}^2\left(\frac{\omega T}{2}\right) \end{aligned} \quad (2.12)$$

The normalized magnitude of the sensitivity transfer function in acceleration, for the AQG, is plotted below:
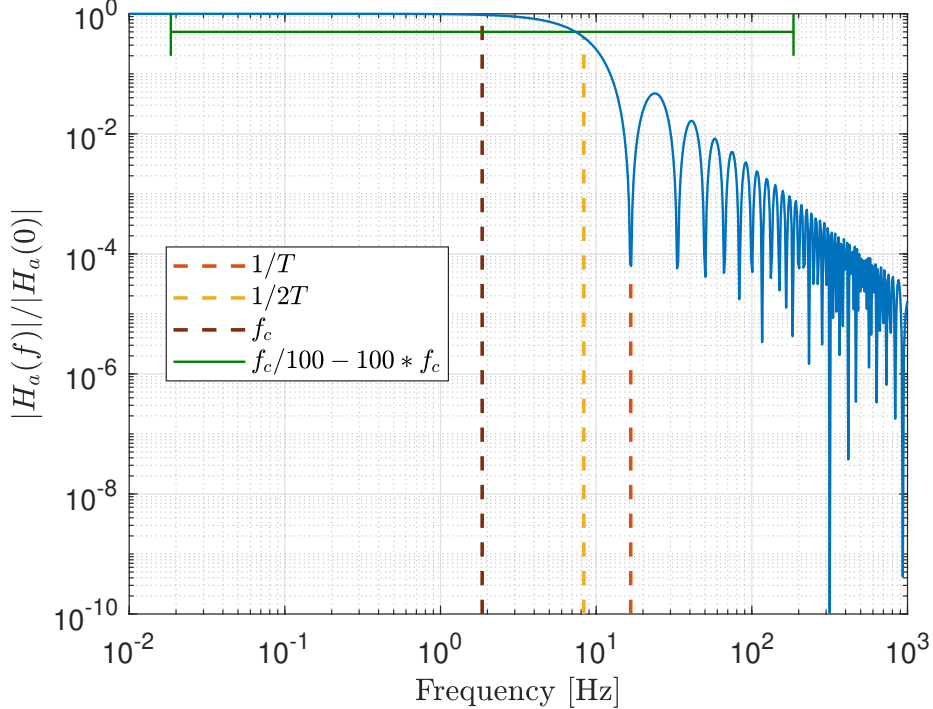
Figure 2.13. Normalized magnitude $|H_a(f)|/|H_a(0)|$ of the AQG's transfer function.

---

[3]The Rabi frequency is a measure of the interaction strength between an atom and an electromagnetic field. In the context of AQG, the Rabi frequency refers to the frequency at which the atoms are driven by the Raman pulses.

This plot provides insights into how vibrations are measured in the AQG [10, 14, 25]. The transfer function exhibits a flat response at low frequencies, and once it reaches the corner frequency $f_0 = 1/2T = 8.33$ Hz, the magnitude decreases by a factor f^{-2}. It resembles the behavior of a second-order low-pass filter. In addition, the sensitivity transfer function has zeros at frequencies that are multiples of $1/(T + 2\tau) \simeq 1/T = 16.67$ Hz.

Such behavior demonstrates that high-frequency vibration noise is well attenuated beyond a certain point. However, for frequencies close but above the cycle frequency $f_c = 1/T_c = 1.85$ Hz, vibrations are not attenuated enough and thus problematic.

On the other hand, low-frequency vibrations are fully measured and transmitted considering the flat response of the sensitivity transfer function at low frequency. The interferometer's sensitivity to the vibrations with a frequency lower than $1/T$ is given by Equation 2.12. When $\omega << 1/T$, it gives $H_a(\omega << 1/T) = k_{\text{eff}}T^2$ [rad/(m/s^2)]. So the sensitivity of the interferometric phase increases quadratically with T at low frequencies [31].

Frequencies below f_c, are considered as gravitational signal [31]. But there is still some vibration noise. It is only for very low frequencies, lower than $f_c/100$ that the vibration noise can be considered negligible, as the random vibration noises that could affect the measurement have typically a lower amplitude than the gravity variations at these frequencies. At these orders of magnitude, some typical effects arise like the tidal and ocean loading effects. Although they do influence gravity, in the context of absolute gravity measurement they are considered as a predictable perturbation. Since they are large compared with the instrumental resolution and targeted precision, they are removed through implemented models [9].

Therefore the vibration noise between $f_c/100$ and $f_c \times 100$ is the main problem in the AQG. Indeed, between $f_c/100$ and f_c, the signal is a mix of gravity signal and vibration noise, and above f_c it is just not well-attenuated vibration noise. Nevertheless, above $f_c \times 100$, vibrations are considered to be efficiently attenuated in the signal by the mirror's sensitivity transfer function. Thus the vibration mitigation in the range $[f_c/100; f_c \times 100]$ is the main direction of improvement in the atom interferometry at present.

Two approaches are commonly used for vibration compensation: vibration isolation and vibration compensation [10]. Vibration isolation aims to attenuate or suppress vibrations by using passive or active isolation platforms. Vibration compensation, on the other hand, records vibrations using additional sensors and removes them from the AQG signal either in real-time or in post-processing. While passive and active isolation platforms will be briefly explained, the vibration compensation technique will receive more detailed attention as this work seeks to enhance the understanding of its implementation.

2.4.1 Vibration isolation

Vibration isolation aims to prevent vibrations from reaching the AQG in order to avoid interferences with the atomic interferometry measurements. Although achieving complete isolation from ground vibrations is practically impossible on Earth, this section discusses two types of platforms that can significantly reduce vibration amplitudes, thereby improving the performance of the AQG.

Passive platform

The passive platform uses an elastic damping material and a mechanical structure to absorb or attenuate mechanical wave vibrations [10]. It typically consists of a mass-spring-damping system, as illustrated in Figure 2.14.
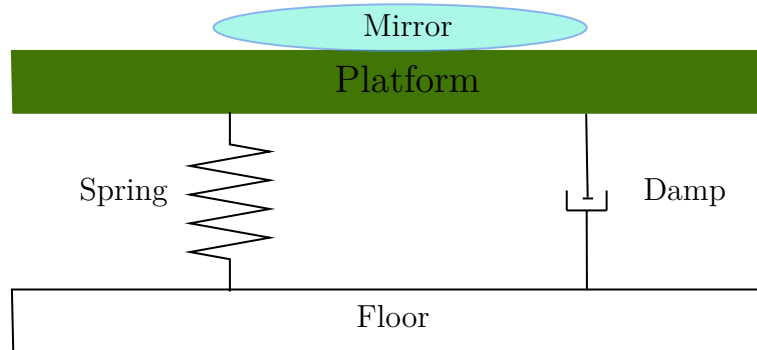
Figure 2.14. Passive platform.

Several studies have explored the use of passive platforms with AQGs. For instance, X. Wu *et al.* [11] achieved a measurement sensitivity of 5000 nm/s^2/$\sqrt{\text{Hz}}$. Passive platforms have certain advantages. They offer simplicity, as they do not require additional sensors, actuators, or control systems. They effectively attenuate high-frequency vibration noise and can withstand heavy loads. However, they are only efficient in suppressing vibrations above their resonance frequency, which is typically around 0.5 Hz. Below this threshold, the platform has no effect or can even slightly amplify the vibrations. A mass-spring-damping system attenuates vibrations above the resonance frequency by a factor f^{-2} but amplifies them around it [14].

Therefore, due to the relatively high resonance frequency of passive platforms, they are not well-suited for AQGs, as low-frequency vibration noise is the most problematic in such instruments. Consequently, passive vibration isolation systems are unable to meet the high-precision requirements of atomic gravimeters.

Active platform

The active platform is an extension of the passive platform, incorporating a control system consisting of one or multiple sensors (such as accelerometers, seismometers, or any inertial sensors) and actuators to respond to disturbances [10]. The additional control system enables a significant reduction in the resonance frequency compared to a simple passive platform. Figure 2.15 illustrates a typical active platform design.
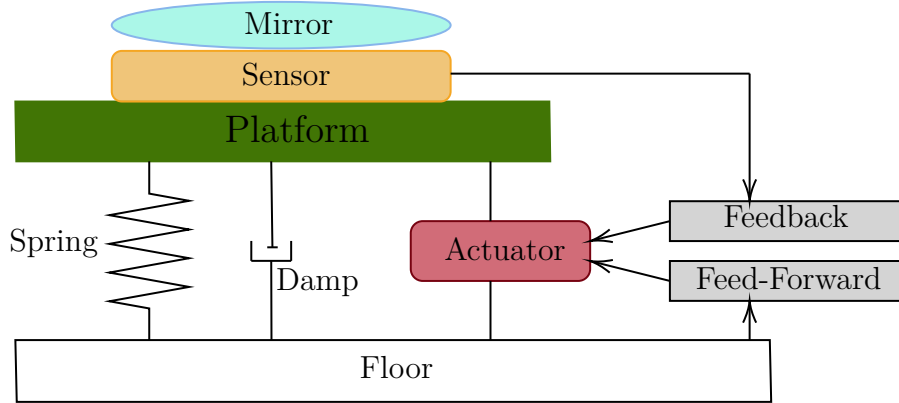
Figure 2.15. Active platform.

Active vibration isolation has been studied more extensively and has demonstrated superior results. M.-K. Zhou *et al.* [12] achieved a better sensitivity of 540 nm/s^2/$\sqrt{\text{Hz}}$, which is almost ten times better than the sensitivity reached with the passive platform [11]. This improvement is attributed to the reduced resonance frequency below 0.02 Hz for the active platform, enabling better attenuation of lower-frequency vibrations typically ranging from 0.1 to 10 Hz. Therefore, active platforms are a suitable choice for AQGs.

Nevertheless, active platforms have certain limitations. They perform poorly in noisy environments with significant vibration levels due to their limited dynamic range. Additionally, the size of the system plays a role, as larger platforms offer better attenuation but are less portable, creating a tradeoff depending on the application. Moreover, the behavior of sensors, actuators, and mechanical components is strongly influenced by environmental conditions such as temperature and pressure.

In summary, active platforms provide significantly improved sensitivity compared to passive platforms. In very quiet environments, it is possible to reach the self-noise of an atomic gravimeter using active platforms. However, they are more suitable for laboratory use and less ideal for portable applications due to the challenges outlined above.

To overcome these limitations, the vibration compensation technique has been explored, which appears to meet the requirements of portability by relying on an additional sensor while providing excellent sensitivity and stability. However, this approach comes with certain costs, as will be discussed in the next section.

2.4.2 Vibration compensation

Vibration compensation aims to mitigate the influence of vibrations on the AQG measurements. This technique involves measuring the raw gravitational signal with the AQG. It means the gravity without any vibration compensation methods, such that vibrations are influencing the measurement and are only attenuated by the mirror, its sensitivity transfer function presented in Figure 2.13. A classical inertial sensor (e.g. seismometer, accelerometer) is positioned as

close as possible to the reflective mirror to measure its vibrations.

The classical inertial sensor signal requires filtering to address issues such as bias drift due to temperature variations, aliasing, or electronic noise [13, 14, 31]. After filtering, the inertial sensor signal can be used. However, since the interferometer signal depends on the difference in position or phase between the three pulses, the sensor signal needs to be converted into a position or phase signal. The conversion is typically done in phase [20, 31, 32]. If the signal is in acceleration, it is weighted by the sensitivity function $f(t)$[4], introduced in Equation 2.10, and integrated over the duration of the atomic interferometer to obtain the vibration-induced phase φ_{vib}:

$$\varphi_{\mathrm{vib}} = k_{\mathrm{eff}} \int_0^{2T} a_{\mathrm{meas}}(t) f(t)\, dt \tag{2.13}$$

Here, a_{meas} represents the acceleration measured by the inertial sensor used for the compensation. The obtained phase is then subtracted from the interferometric phase as it is considered as noise (see Equation 2.7).

Real-time and post-processing compensation differ in how they handle φ_{vib}. In real-time compensation, a phase correction corresponding to φ_{vib} is applied to the Raman lasers just before the last pulse of the interferometer [8, 10]. On the other hand, post-processing compensation involves converting the acceleration measurements from gravity and vibrations into phases, compensating for them, and then converting them back into accelerations [13, 14]. The simplified process of vibration compensation is depicted in Figure 2.16.
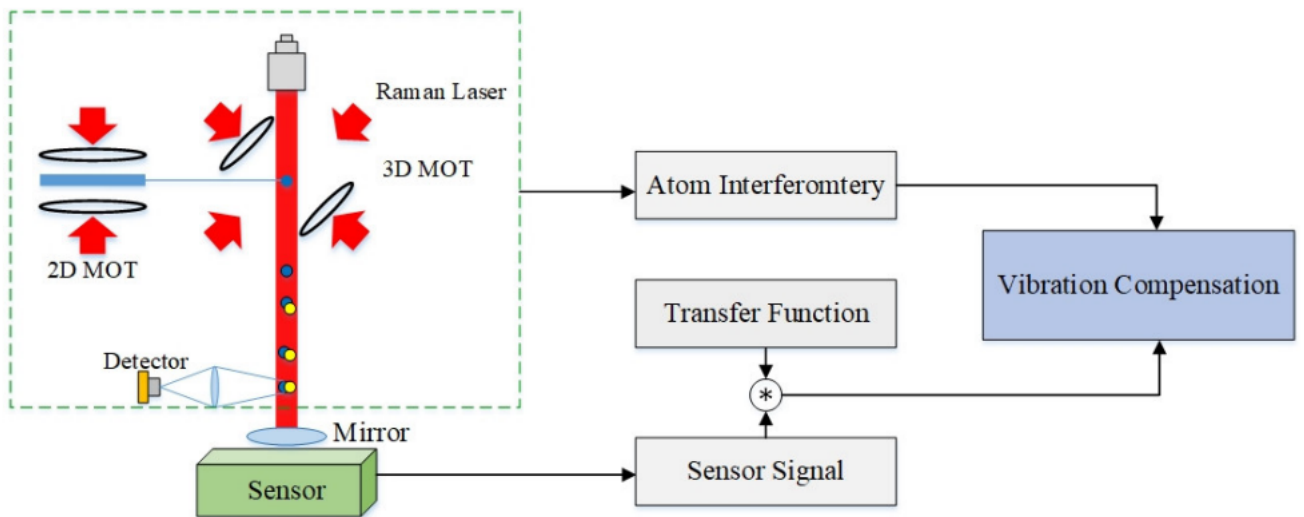
Figure 2.16. Simplified process of vibration compensation. Figure from [10]

The advantages of vibration compensation over vibration isolation include the following [10]:

- Vibration compensation only requires the measurement of vibrations using a sensor,

---

[4]If it is a velocity signal, the sensitivity function is different but since an accelerometer is used in the measurements, only accelerations are studied.

eliminating the need for heavy mechanical isolation devices. It enables smaller, lighter, and quicker installation of the AQG.

- Vibration compensation effectively reduces the impact of vibrations at all frequencies within its bandwidth. Unlike platforms that exhibit a low-pass effect and thus an attenuation dependent on the frequency. Vibration compensation addresses vibrations equally at all frequencies within its bandwidth.

- Real-time compensation provides better vibration attenuation in harsh environments where disturbances are significant, as it compensates at each measurement. However, post-processing compensation can only be used in relatively calm locations because vibrations causing a change in the interferometric phase of more than π result in fringe jamming in the interferometric pattern and thereby unreadable data.

Nevertheless, implementing vibration compensation comes with challenges. It requires significant computational resources to determine the sensitivity function of the AQG and its Fourier transform accurately. Additionally, obtaining precise vibration measurements at low frequencies using accelerometers is challenging due to their typical high drift at low-frequency. Furthermore, the accelerometer should ideally be clamped to the reflective mirror, but it is often impractical, resulting in a small difference between the measured vibrations and the actual vibrations experienced by the mirror. Moreover, depending on the atomic gravimeter design, fixing a sensor close to the mirror can be difficult and may require additional support structures.

Currently, most researchers are focusing on real-time compensation due to its performance and robustness, even in harsh environments. Various studies have implemented either post-processing or real-time compensation techniques. For post-processing compensation, the work of L. Richardson [14] and Le Gouët *et al.* [15] have explored this technique and achieved good results. Similarly, for real-time compensation, studies by F. Yver-Leduc *et al.* [13] and V. Ménoret *et al.* [8], among others, have demonstrated its effectiveness. In general, in a seismic calm environment, the post-processing compensation will be slightly more accurate than the real-time one. Indeed, in the real-time compensation, the last few µs of the interferometer are not taken into account in the vibration compensation, as the accelerometer signal needs to be processed, and injected in the Raman laser before the last pulse. But it is the price to pay for a more robust compensation.

Chapter 3

Vibration compensation with Titan

As discussed in the previous section, vibration compensation is a complex process. In order to gain a comprehensive understanding of this technique and improve it in future iterations, the PML aims to analyze the signals from the accelerometer Titan and the AQG, using MATLAB software, to understand their relationship. To achieve this objective, an in-depth analysis of the gravity signals obtained at the output of the AQG is carried out, along with a discussion of the limitations encountered. Since the vibration compensation already implemented in the AQG is in real-time and uses the accelerometer Titan, the sensor's characteristics are reviewed and the reasons for its usage are explained. Once the sensor has been reviewed, it is possible to dive into the whole compensation process. The filters applied on the Titan signal are presented as well as the reasons for them. In the next step, the separated signals from AQG and from Titan are analyzed, along with the effect of vibrations on them. It opens up the understanding of the correlation between the two signals.

The results are validated by analyzing the Titan signals more in-depth and by comparing them with two additional seismometers. It gives insight into how the ground vibrations are felt by the AQG and it validates the Titan results.

Finally, some attempts at a post-compensation process are presented along with the conclusions that can be extracted from it.

3.1   Gravity signal analysis

In this first section, an analysis of typical measurements output by the AQG in the user interface is performed. Figure 3.1a shows the time series of gravity measurement after correction of systematic effects, while Figure 3.1b displays the time series without any corrections. The gravity measurement was carried out with the AQG in Liège during the weekend from March 18, 2023, 00:00 to March 20, 2023, 00:00.
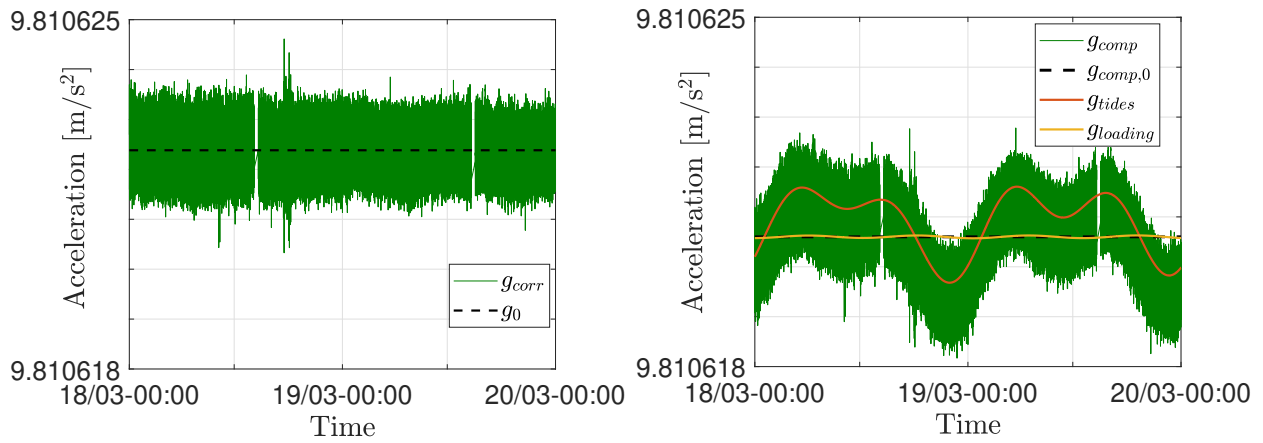
(a) With vibration compensation and gravity correction.

(b) With vibration compensation only.

Figure 3.1. Time series of a gravity measurement from AQG, the black dashed line is the mean in both cases. 18/03/2023 00:00 to 20/03/2023 00:00 in PML Liège.

In the corrected time series plot, gravity values oscillate around the average value $g_0 = 9.810622383$ m/s^2, which is continuously updated with each new measurement, becoming more accurate with longer integration times (continuous averaging). The measured gravitational signal is compensated for vibrations (g_{comp}) and corrected for other factors such as tides, ocean loading effects, and various gravity variations due to systematic effects measured by control sensors (e.g., tilt, pressure, laser noise) or not (g_{syst}). The corrected gravity signal, denoted as g_{corr}, can be calculated using the following equation:

$$g_{\text{corr}} = g_{\text{comp}} - (g_{\text{quartz}} + g_{\text{tilt}} + g_{\text{pressure}} + g_{\text{tide}} + g_{\text{syst}} + g_{\text{height}} + g_{\text{laser}} + g_{\text{polar}}) \tag{3.1}$$

As explained in Section 2.4, the ocean loading effect and the tidal effect have a significant impact on the measurement. It can be seen in Figure 3.1b which shows the uncorrected measurement of g. Only variations due to tides (g_{tides}) and ocean loading effects (g_{loading}) have been displayed but all the effects in Equation 3.1 are corrected. They are corrected based on models or sensor measurements (e.g. tiltmeter, barometer, etc.). Typically, for tides and ocean loading, the software Tsoft is used to evaluate and correct them. The mean of the uncorrected measurement, $g_{\text{comp,0}}$, is different from the one of the corrected time series, which shows the importance of these effects on gravity and how they hide the smaller variations which are interesting in the study of vibrations.

The variations observed around the mean value in Figure 3.1a are a combination of noise from the measurement system, vibrations, and actual changes in gravity. In the specific measurement shown in the figure, an interesting effect is observed—an increase in vibration amplitude around 18:00 on March 18. This effect is probably due to an earthquake. Looking at Volcano Discovery's earthquake data, it can be seen that the seismic activity peaked around 17:30 on March 18 due to a magnitude 6.8 earthquake in Ecuador. It seems very likely that this earthquake was the cause of this peak. It was probably possible to see it since March 18 and 19 were a weekend, thus the University during a weekend is seismically calm compare to a working day as almost no vibrations due to human activities impact the measurement and

thus the natural cause of an earthquake seems plausible. It also explains the fact that there are no differences in the vibrations between day and night, which is not the case during a working week.

Daily gaps are also observed in the measurement, they correspond to AQG's auto-calibration processes. During a calibration period, no data are measured, so these gaps are not taken into account in the PSD or the mean calculation. Reminders on the PSD can be found in the Annexe A.

To focus on the variable component of the graviational signal, it is common to work with the residual gravity (g_{res}), obtained by removing the mean value (g_0) from the corrected signal (g_{corr}):

$$g_{\mathrm{res}} = g_{\mathrm{corr}} - g_0 \tag{3.2}$$

Working with the residual gravity is convenient because it eliminates the continuous component when calculating the PSD or ASD (Amplitude Spectral Density) of the signal. Therefore, the PSD presented in Figure 3.2 represents the PSD of g_{res}.
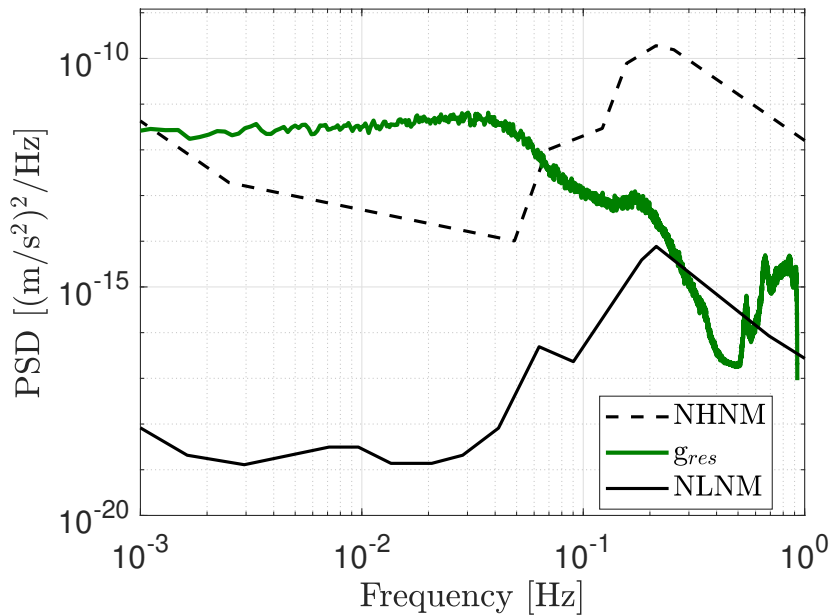
Figure 3.2. PSD of the residual gravity. 18/03/2023 00:00 to 20/03/2023 00:00 in PML Liège.

Figure 3.2 shows the PSD of ground vibrations measured in Liège within the frequency range of $0.001 - 1$ Hz. It also includes the NHNM (New High Noise Model) and NLNM (New Low Noise Model) curves. They represent, respectively, the highest and lowest vibration accelerations due to seismic motions of the Earth. These curves were derived from numerous measurements collected in low-vibration environments by J. Peterson [33].

Looking at the PSD of the residual gravity in green, at low frequencies, it exhibits a relatively flat and slow-varying behavior. This region corresponds to ambient seismic noise from various sources, including natural geological processes and human activities. It is commonly associated with white noise characteristics, indicating a random distribution of energy across frequencies.

A notable feature in the PSD is a small peak observed around 0.15 Hz, as the PSD is decreasing, known as the micro-seismic peak. It originates from natural sources deep within the Earth's crust, and results from processes such as tectonic plate movements or oceanic wave interactions. The micro-seismic peak appears as a localized increase in power at this specific frequency [34, 35].

Following the micro-seismic peak, as the frequency increases, the PSD keeps decreasing due to the working principle of the AQG. The drop at 0.5 Hz is visible in every PSDs obtained with the AQG and comes from the tracking of g through the servo-loop on the chirp α explained in Section 2.2. It is not a physical signal that can be analyzed.

It is important to note the presence of two additional small peaks when the PSD rises again above 0.5 Hz. They are not always present and the reason for their presence is not precisely known but considering that this occurred over a weekend, the cause of human activities is unlikely. A potential explanation is the peak in seismic activity due to the earthquake in Ecuador. However, earthquakes usually modify the PSD by increasing the white noise plateau, still resonances in the building due to the earthquake's vibrations could have caused these peaks. Other explanations could be the presence of strong winds which induce resonances in the building at these frequencies, construction in the building, or simply defects in the AQG's internal system.

When comparing with a typical signal during a very calm period at the University of Liège (Easter vacation), it is possible to point out the differences.
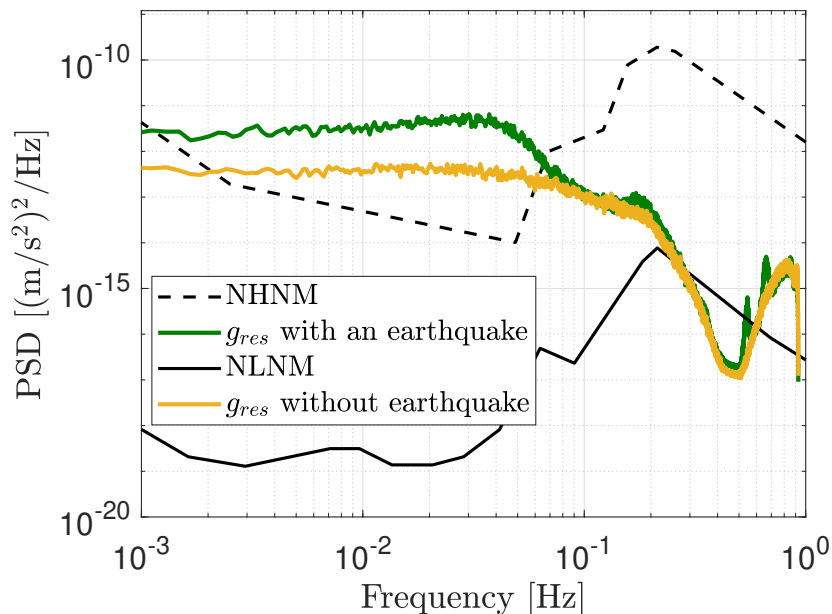
Figure 3.3. Comparison of residual gravity's PSDs between a measurement with an earthquake and one without. Earthquake: 18/03/2023 00:00 to 20/03/2023 00:00 and without earthquake: 15/04/2023 00:00 to 17/04/2023 00:00, both in PML Liège.

In Figure 3.3, some observations can be made. The measurement during the Easter break has a very smooth and typical PSD for an AQG. While the one from March 18 with the earthquake

shows an increase in the white noise plateau at low frequency as well as a non-smooth decrease towards the zero at 0.5 Hz. It is probably due to the increase in the seismic activity and thus a stronger micro-seismic peak at 0.15 Hz. It proves the influence of earthquakes on the gravitational PSD.

Overall, the PSD of ground vibrations in Liège between March 18 and 20 exhibits a complex pattern, characterized by low-frequency ambient seismic noise, a distinct micro-seismic peak around 0.15 Hz, and variations influenced by the working principle of the AQG. The presence of additional peaks whose origin is not known yet highlights the dynamic nature of ground vibrations and the influence of geological, and meteorological processes on the measured data.

To assess the performance of gravity measurements, a typical effective tool used in gravimetry is the Allan deviation. This metric quantifies the frequency stability of a signal in the time domain and provides insights into noise sources originating from random processes (e.g., bias drift, white noise, quantization noise, etc.). More information about the Allan deviation can be found in Annexe B. Figure 3.4 presents the Allan deviation of the residual gravity signal.
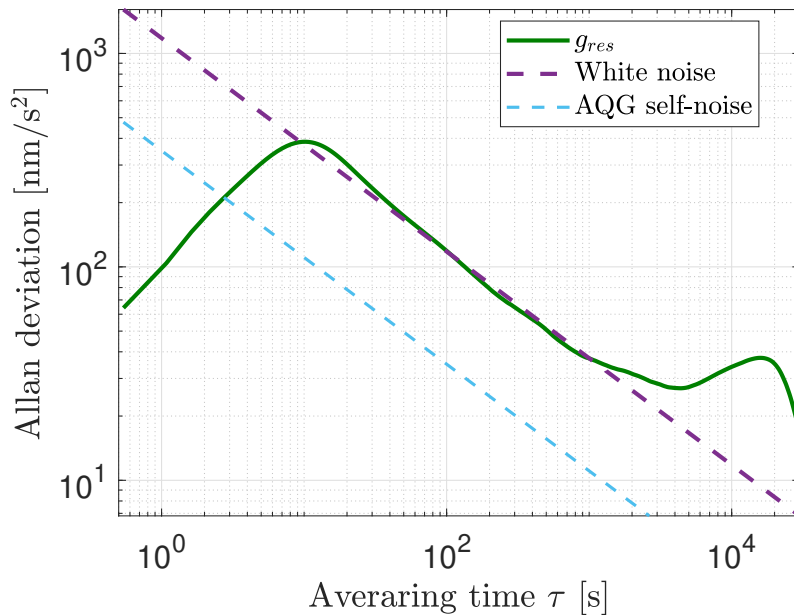
Figure 3.4. Allan deviation of the corrected residual gravity signal. 18/03/2023 00:00 to 20/03/2023 00:00 in PML Liège.

In an Allan plot, the τ axis can be interpreted as a frequency axis reverted. A small τ corresponds to a short averaging time, which better represents high-frequency noise, while a longer τ describes low-frequency noise. Therefore a link exists between the Allan deviation and the PSD of a signal.

In the case of the Allan deviation plot in Figure 3.4, the curve initially increases with increasing τ, this effect is once again due to the tracking of g and the servo-lock of α to have the null interferometric phase. This part of the plot does not have any physical interpretation.

Then it reaches a transition point around 10 s and enters the white noise region at about

$\tau = 30$ s. In this region, the Allan deviation typically has a slope of $-1/2$ in the log-log plot. Such a slope is characterized by the dashed purple line "White noise" in the plot, which represents the behavior of white noise. The value of the dashed purple slope taken at $\tau = 1$ s defines the sensitivity of the instrument, representing the statistical uncertainty obtained after averaging over 1 s. In this case, its value at $\tau = 1$ s is 1180 $(\text{nm/s}^2)/\sqrt{\text{Hz}}$ and it can be verified in Figure 3.2 of the PSD since the relationship between the sensitivity $\mathcal{S}$ and the PSD of the white noise region S is $S = 2\mathcal{S}^2$ [8], here $S = 2.7848 \times 10^{-12}$ $(\text{m/s}^2)^2/\text{Hz}$. It is known that the AQG self-noise limits the sensitivity at 350 $\text{nm/s}^2/\sqrt{\text{Hz}}$, which is represented by the light blue dashed line in the plot. In the measurement obtained, the sensitivity limit is three times worse than the self-noise limit, even with vibration compensation. It, therefore, shows that improvements in the vibration compensation technique implemented can be achieved. The white noise region in the Allan plot corresponds to the white noise region between 0.001 and 0.04 Hz in the PSD in Figure 3.2, the dominant noise sources are uncorrelated and exhibit a relatively constant level of noise power spectral density in this region. The Allan deviation decreases as the averaging time increases as longer averaging intervals allow for better cancellation of uncorrelated noise, thus improving precision.

After the white noise region, the Allan deviation shows a small bump. This bump is always found at the end of the Allan deviation of any measurement, so if a longer measurement is taken, the bump will appear further out. The cause of this bump is not known yet, the AQG's Allan deviation is supposed to continuously decrease over time as the AQG does not show any drift, it is ensured by Exail. Therefore this bump is still being investigated.

The long-term stability corresponds to the lowest point of the curve, in this case, 17 nm/s^2. It means that the measurement obtained is correct at ± 17 nm/s^2.

For the sake of comparison, the Allan deviation of the uncorrected measurement shows much poorer stability. Figure 3.5 illustrates it.
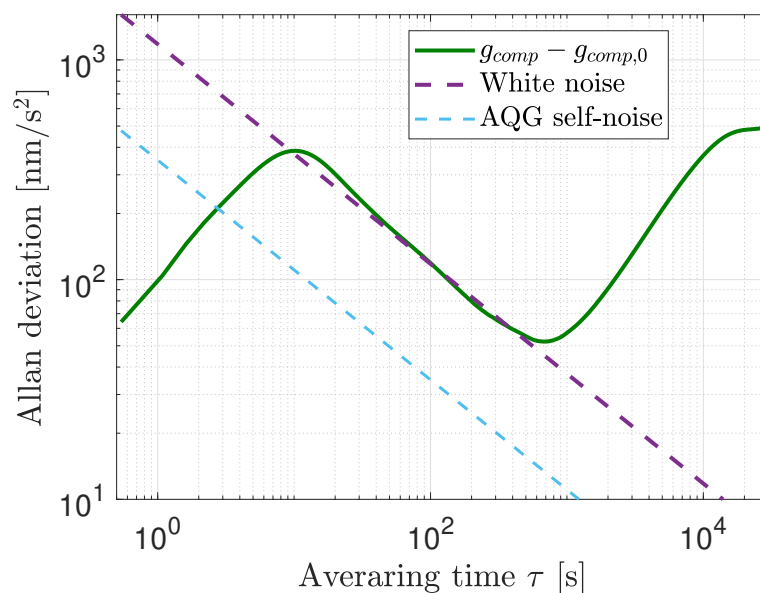
Figure 3.5. Allan deviation of the uncorrected residual gravity. 18/03/2023 00:00 to 20/03/2023 00:00 in PML Liège.

In this case, the tidal effect at low frequency is clearly visible, as the Allan deviation increases at low frequency. Compared to the Allan deviation in Figure 3.4, stability is only 52.3 nm/s^2. Additionally, there is strong drift after the white noise region since the Allan deviation increases with a slope of +1 in the log-log plot.

This preliminary analysis gives a global picture of gravity measurement. However, the hidden part of all this is the vibration compensation. In the following sections, the real-time compensation developed by Exail will be analyzed thoroughly as well as how vibrations impact the AQG. Finally, attempts to implement our own compensation algorithm are presented.

3.2 The accelerometer Titan

The Titan accelerometer, designed by Nanometrics is an integral component of the AQG system for vibration compensation. The accelerometer datasheet can be found on Nanometrics' website [36], and the key information is summarized below.

The Titan accelerometer offers a selectable full-scale range. For vibration measurements, it has been set to $\pm 0.25g$ peak, which is the smallest range available. It ensures the lowest possible self-noise for the sensor, as shown in Figure 3.6.
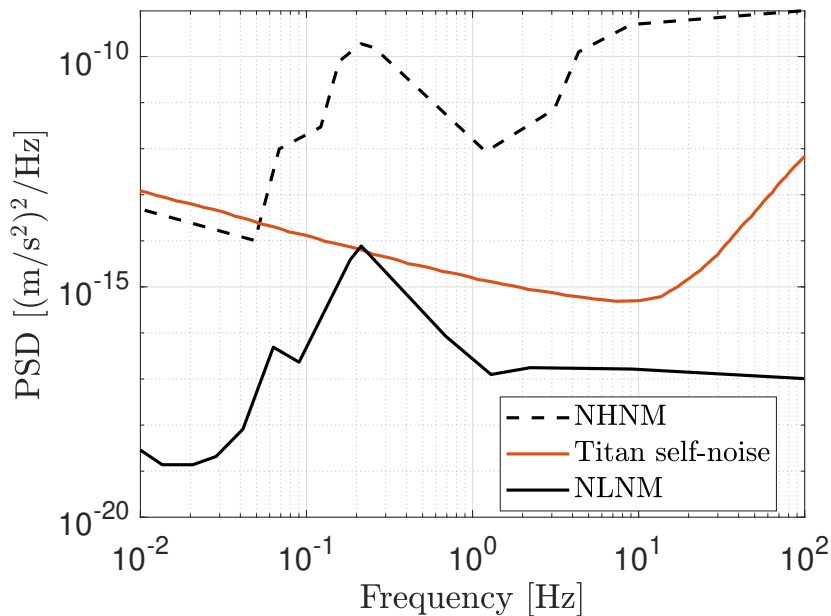
Figure 3.6. Titan's self-noise PSD.

To assess the Titan accelerometer's performance in vibration measurements, a comparison can be made using the NHNM and NLNM curves. In general, vibrations in normal laboratory conditions far exceed the NHNM curve due to human-induced vibrations at frequencies higher

than 10 Hz (e.g., walking, cars, air conditioning systems). However, at low frequencies, it is not guaranteed. Therefore, the Titan's self-noise, within the working frequency range 0.01-10 Hz, might limit the AQG.

In order to ensure that it is not the case, the gravity data (g_{res}) and the self-noise of the Titan are compared, with the self-noise being multiplied by the sensitivity transfer function of the AQG. This multiplication enables a meaningful comparison since both quantities will integrate the sensitivity transfer function of the AQG in their signals. Indeed, the gravitational signal obtained with the AQG includes its sensitivity function in its physical signal. The PSD and Allan deviation of the two signals are presented in Figures 3.7a and 3.7b, respectively.

(a) PSD

(b) Allan deviation
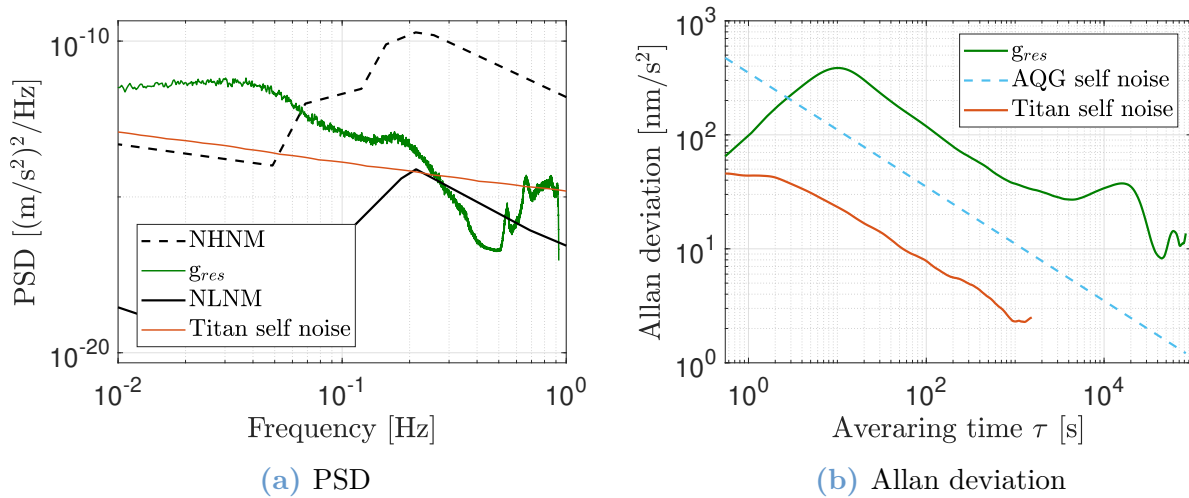
Figure 3.7. Comparison between the residual gravity (g_{res}) and the Titan's self-noise. The Titan's self-noise incorporates the sensitivity transfer function of the AQG.

Upon analyzing the PSD, it appears that the Titan's self-noise exceeds the residual gravity's PSD above 0.3 Hz. However, as previously discussed, the PSD of g_{res} in this range is not physically meaningful, indicating that the Titan's self-noise does not have any influence on this non-physical part of the signal. At lower frequencies, which correspond to the physical part of the gravitational signal, the PSD of the Titan's self-noise remains lower than that of the residual gravity.

To provide a clearer visualization, the Allan deviation plot was generated. It effectively demonstrates that the white noise region of the Titan's self-noise is significantly lower than that of the AQG self-noise. Consequently, the sensitivity of the Titan accelerometer should not limit the AQG measurements, as the AQG signal will reach its self-noise limit prior to that. This assertion will be validated using the IGOR platform in Section 4.1, where the gravity measurement reaches the AQG self-noise.

To obtain the Allan deviation plot, a time series is required. However, since only the PSD is provided for the self-noise of the Titan, a technique is used to estimate the Allan deviation. This approach involves filtering a white noise time series to match the desired signal's PSD and then computing the Allan deviation of the time series obtained. This method was used to determine the Allan deviation of the Titan's self-noise.

The Titan accelerometer has a bandwidth from DC to 430 Hz, which is defined by its transfer function. The zeros and poles of the transfer function are provided by the manufacturer, and its Bode diagram is illustrated in Figure 3.8. The magnitude reaches -3 dB at the cutoff frequency of 430 Hz, and a resonance frequency is visible around 140 Hz. A phase drop of $450°$ (equivalent to $5\pi/2$) can be observed at the cutoff frequency. The output sensitivity of the Titan accelerometer is 8.16 V/(m/s^2).
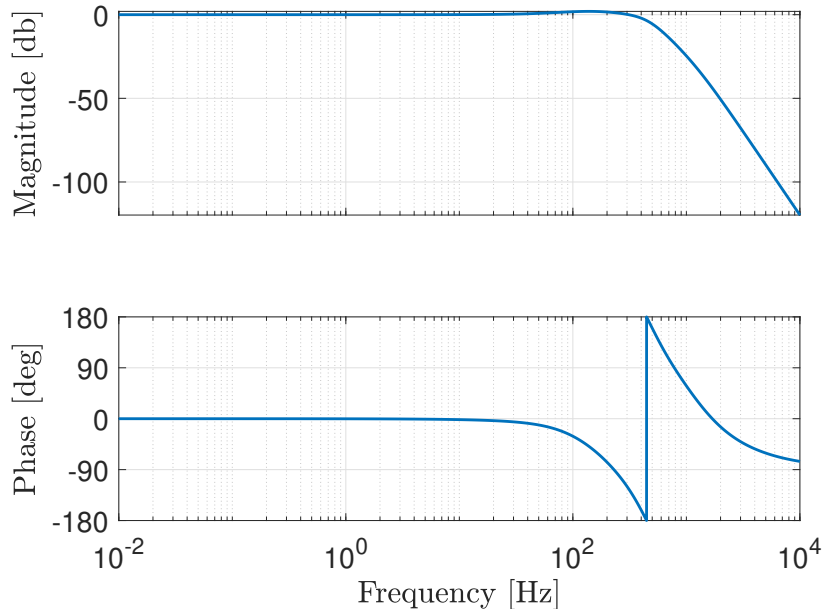
Figure 3.8. Titan's transfer function.

3.3   Real-time compensation analysis

For real-time compensation, the Titan signal undergoes a series of filtering operations, after which it is multiplied by the sensitivity function and integrated to obtain the compensation phase. The compensation phase is then injected into the Raman laser before the third pulse as explained in Section 2.4.2. The acquisition chain through which the Titan signal needs to go through [31] is depicted in Figure 3.9.

The signal is first amplified by an operational amplifier with a gain of 16.09. Accelerometers often exhibit bias drift, which is a slow change in the offset over time due to various factors such as temperature and acceleration changes. To eliminate the bias drift effect in Titan, a second-order high-pass filter with a cutoff frequency $f_{hp} = 0.05$ Hz is applied to the signal. It eliminates the offset and retains only the varying components while suppressing slow frequency drifts caused by temperature dependencies.

The frequency response and self-noise of the Titan are determined by its internal structure, setting the range of frequencies it can accurately measure. However, signals outside this range can still influence the vibration compensation. To correct it, the accelerometer signal is low-pass filtered through a second-order Sallen-Key filter. The Sallen-Key filter is chosen for its advantages over a normal low-pass filter. It offers simplicity, flexibility, and stability thanks to its minimal component count and use of op-amps. The filter exhibits low distortion,

Figure 3.9. Acquisition chain for Titan.

making it suitable for preserving signal integrity. The cutoff frequency of the low-pass filter is typically several orders of magnitude higher than $f_0 = 1/2T$ to properly compensate for the vibrations that still partially affect the AQG measurements. The cutoff frequency must also be lower than the sensor's maximum detectable frequency, defined by the sampling frequency and the Nyquist theorem ($f_{max} = f_s/2$). For Titan, the cutoff frequency has been fixed to $f_{lp} = 1061$ Hz.

Another factor to consider is aliasing, caused by the limited sampling frequency. If the sampling frequency is at least twice as high as the highest frequency present in the signal, no problems arise. However, when this condition is not met, the sampled signal is not accurately reconstructed. Not only does it lose information on frequencies higher than $f_s/2$, but it also interprets them as lower frequencies. While the low-pass filter implemented already helps mitigate the aliasing effect, an anti-aliasing filter can be implemented as an additional precaution, although it is essentially a low-pass filter as well. For Titan, the cutoff frequency of the anti-aliasing filter has been fixed to $f_{aa} = 10610$ Hz.

The cutoff frequencies were determined by Exail after extensive testing and gave the best results. The filtering chain is implemented in hardware on the acquisition board, and the signal is subsequently digitized using a low-noise 24-bit ADC at a sampling rate of 50 kHz.

Once digitized, the signal is "downsampled" to 5 kHz, which is achieved by summing over 10 samples by Exail (similar to averaging). The downsampling yields a gain of 10. A DC block is then applied to remove any remaining components below 0.02 Hz to completely suppress
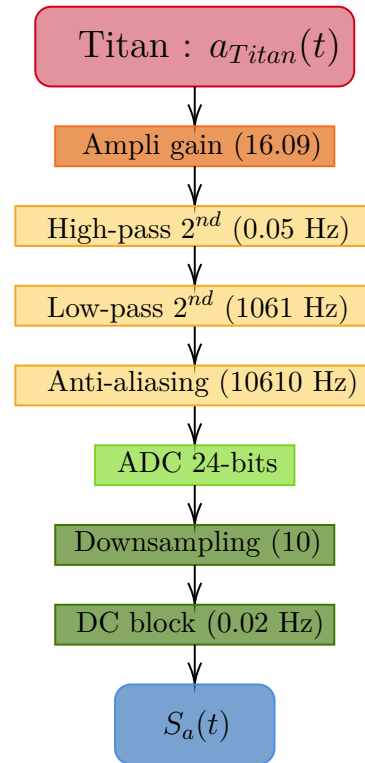
drift influence. The resulting digital signal $S_a(t)$ is given by:

$$S_a(t) = 10 G S \tilde{a}_{\text{Titan}}(t) \tag{3.3}$$

Here, the downsampling factor is denoted by 10, $G = 16.09$ represents the gain of the operational amplifier used, and $S = 8.16$ V/(m/s^2) corresponds to the sensor's sensitivity. $\tilde{a}_{\text{Titan}}(t)$ denotes the acceleration measured by the Titan accelerometer after the filtering stage. It is assumed that the displacement measured by the Titan corresponds to that of the reflective mirror in the AQG, affected by the Titan's transfer function.

Due to the presence of analog filters, the overall transfer function $H(j\omega)$ of the signal is not solely determined by the Titan accelerometer, but rather by a combination of multiple transfer functions:

$$H(j\omega) = H_{\text{Titan}}(j\omega) H_{\text{HPF}}(j\omega) H_{\text{LPF}}(j\omega) H_{\text{AA}}(j\omega) \tag{3.4}$$

Here, $H_{\text{Titan}}(j\omega)$ represents the transfer function of the Titan accelerometer as described in the previous section. $H_{\text{HPF}}(j\omega) = \frac{(j\omega)^2}{(\omega_{\text{hp}} + j\omega)^2}$ denotes the second-order high-pass filter with the cutoff angular frequency $\omega_{\text{hp}} = 2\pi \times 0.05$ rad/s. H_{LPF} corresponds to the second-order Sallen-Key low-pass filter with a cutoff angular frequency at $\omega_{\text{lp}} = 2\pi \times 1061$ rad/s. Finally, $H_{\text{AA}}(j\omega) = \frac{\omega_{\text{aa}}}{\omega_{\text{aa}} + j\omega}$ represents the anti-aliasing filter with the cutoff angular frequency $\omega_{\text{aa}} = 2\pi \times 10610$ rad/s.

A comparison between the total transfer function and the transfer function of the Titan accelerometer alone is illustrated in Figure 3.10.

Figure 3.10. Comparison between the full transfer function (Titan+3 analog filters) $H(j\omega)$ and the transfer function of the Titan accelerometer alone $H_{\text{Titan}}(j\omega)$.

The issue with all the additional filters is that they introduce frequency-dependent phase shifts, with the result that the acquired signal does not accurately represent the actual vibrations

experienced by the AQG mirror. The most straightforward solution to suppress these phase shifts would be to remove the effect of all the filters by deconvolving the acquired signal with the acquisiti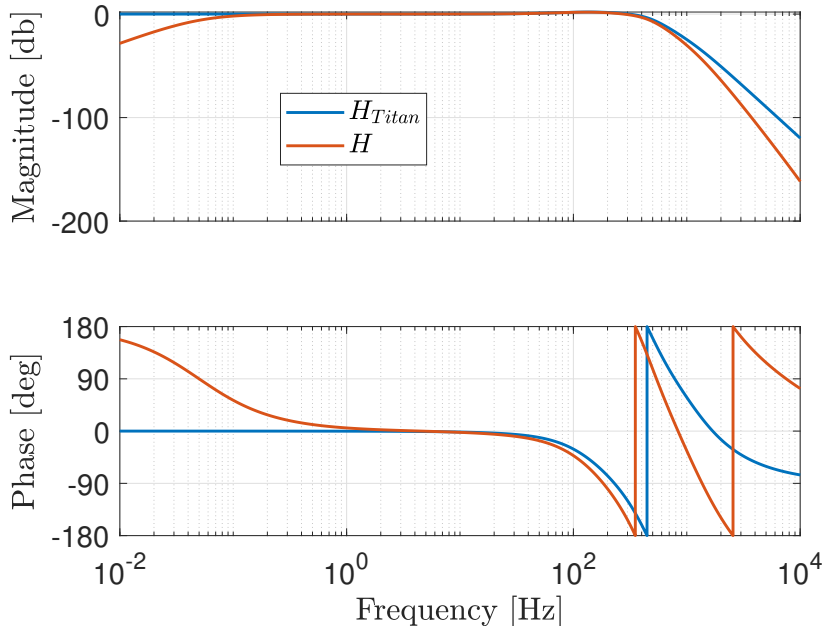on transfer function $H(j\omega)$. However, this approach is computationally intensive and not feasible for real-time compensation, which requires fast processing.

Exail addressed the problem by incorporating an averaged delay, denoted as δt, into the signal [20]. The delay is averaged because it is not possible to have different delays for different frequencies due to varying phase shifts. Therefore, an average delay is computed. It represents a perfect delay only for a specific frequency but still minimizes variations caused by vibrations in the gravity measurement. Since the measured vibrations used in the compensation are weighted by the sensitivity function $f(t)$ of the AQG (which is zero outside the window $[0, 2T]$), the delay is incorporated by shifting the window by the corresponding delay $[0 + \delta t, 2T + \delta t]$. The optimal delay δt can be determined using the method proposed by V. Ménoret [37].

Exail has implemented the real-time compensation approach, but it is complex and the multiple filters still have an influence, as their induced phase shifts are not fully compensated by the averaged delay. Furthermore, the filters were chosen on the basis of multiple tests, and there is no theoretical analysis that justifies their designs yet. To gain a full understanding of the compensation process based on Titan, a thorough review of the signals and processes should be conducted at PML before attempting any modifications.

Correlation between Titan and AQG signals

To assess how vibrations affect the AQG, separate measurements of the AQG without compensation and the Titan accelerometer are obtained. The objective is to determine whether there is a correlation between the accelerations measured by the Titan and the AQG, enabling a simpler analysis based on accelerations rather than on less intuitive phase measurements.

The comparison between the AQG measurement with and without vibration compensation is shown in Figure 3.11a.[1]

---

[1]The measurements realized in the following are always below 1h, as larger data set can become long or impossible to process, especially with the 50 kHz of Titan. Also, the AQG cannot run without vibration compensation for too long otherwise it will deviate and thus stop the measurement to recalibrate.

(a) Time series

(b) ASD

(c) Allan deviation
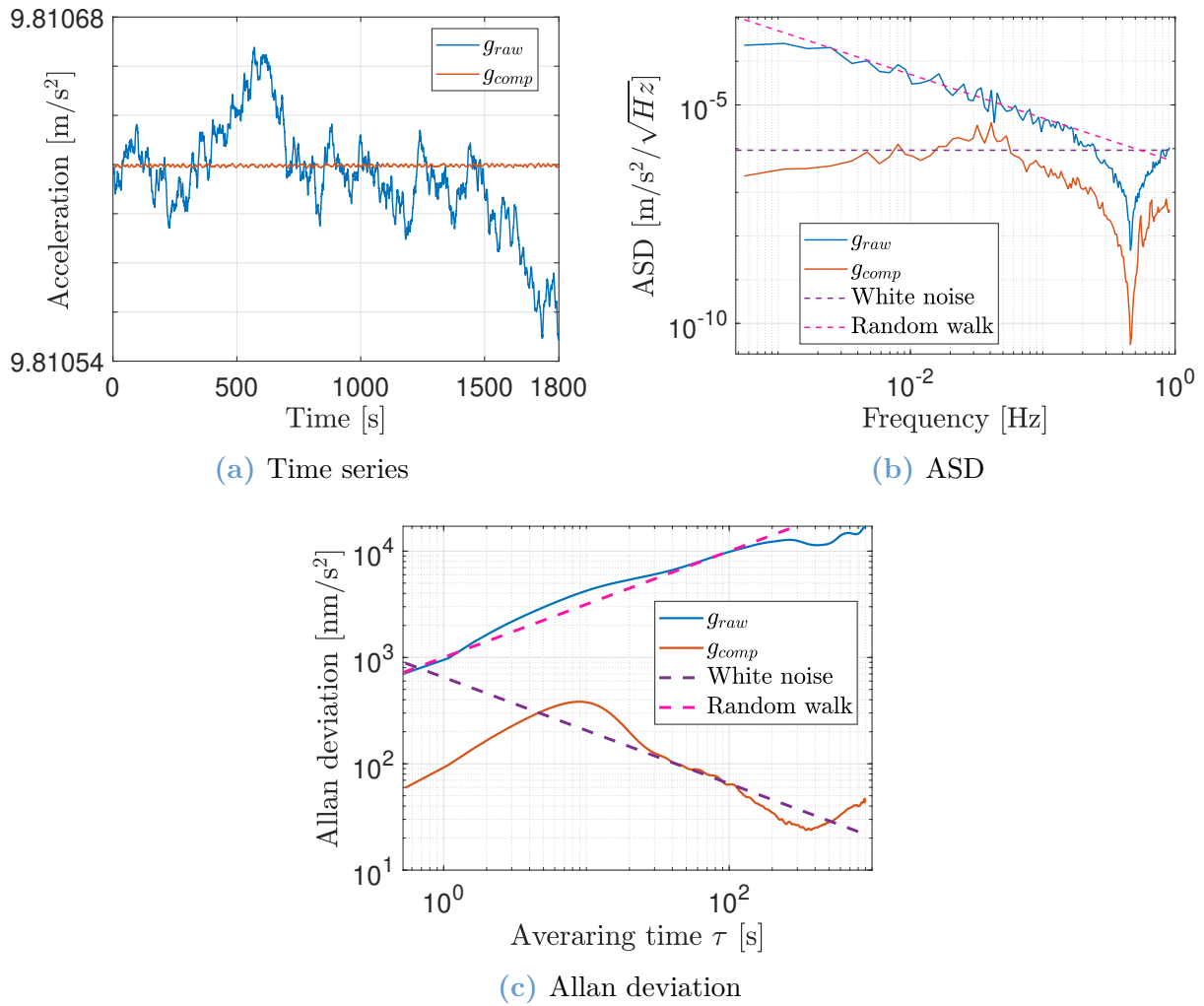
Figure 3.11. Comparison of an AQG measurement with (g_{comp}) and without (g_{raw}) vibration compensation. g_{comp} : 20/03/2023 at night and g_{raw} : 02/04/2023 at night, both in PML Liège.

In the time series plot, it is evident that the variations in gravity measured are much larger without compensation. This effect is also observed in the ASD plot, where the amplitude at each frequency is higher for the raw measurement. Additionally, it is worth noting that the ASD in Figure 3.11b shows a steeper drop than the PSD shown in Figure 3.2 (The ASD is essentially the square root of the PSD, thus they can be compared). It is due to the shorter measurement duration and thereby fewer data points available to obtain a smooth curve.

In the ASD and the Allan deviation plots, two interesting features are represented. First, the mean of the white noise region in the compensated measurement is highlighted with the dashed purple line, it amounts to 9.19×10^{-7} m/s^2/$\sqrt{\text{Hz}}$. Thus in the Allan deviation plot, such a white noise translates into a slope of $-1/2$ as discussed in Section 3.1. The second feature is the Random walk noise that is present in the raw non-compensated measurement. It is a noise where one data point is related to the previous by a random step. In ASD it is represented by a typical curve decreasing in $1/f$ (often it is expressed in terms of PSD as a $1/f^2$ noise), it can be seen that the ASD of the raw measurement nicely follows such a

behavior. The Randow walk noise is represented by a slope of $+1/2$ in the Allan deviation plot as represented by the dashed pink line.

What can be deduced from the comparison between a measurement with and without vibration compensation, is that vibrations strongly disrupt the AQG measurements by inducing Random walk noise. Consequently, all its groundbreaking performances are washed away as it has no long-term stability and its sensitivity is not measurable.

Before finding the correlation between the Titan and the AQG, the typical signal obtained with Titan needs to be analyzed. An initial challenge encountered in this study for the Titan measurement was the inability to record the Titan's signal using an external real-time recorder due to ADC noise limitations at low frequencies. Despite testing various recorders, no satisfactory results were obtained. Consequently, the Titan signal had to be acquired through the Exail acquisition board, which includes the applied analog filters. Although the filters can be easily removed in the frequency domain, the procedure is harder in the time domain. Hence, all the time series presented here represent the filtered signal, providing a useful indication of the signal's amplitude only since nothing else can really be extracted from these plots anyway. The frequency domain plots, however, show the signal without the filter's effects and the sensor's transfer function behavior. It is the case for every plot in this thesis. A typical Titan signal is depicted in Figure 3.12.

(a) Time series

(b) ASD
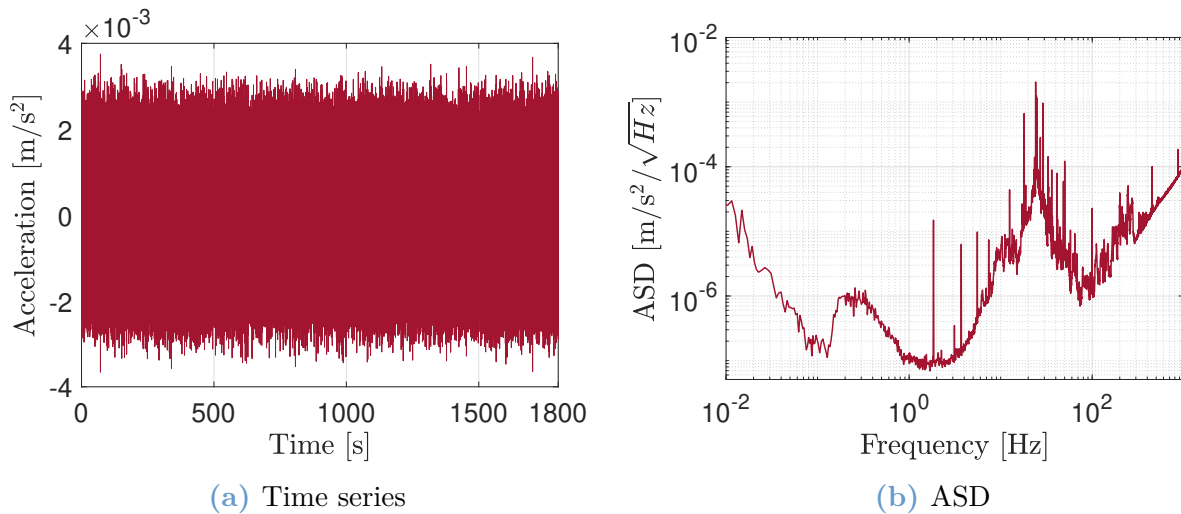
Figure 3.12. Typical vibrations measurement with Titan. 02/04/2023 at night in PML Liège.

From the time series, as expected, nothing can really be extracted except the fact that the amplitude of the vibrations (at night here) is comprised between ± 4 mm/s^2. In Figure 3.12b, the signal exhibits an increase at very low frequencies, below 0.05 Hz Titan is greatly influenced by drift (it is not visible in the time series plot as it has been filtered already). The micro-seismic peak is observed at around 0.15 Hz. Between 10-100 Hz, high levels of vibrations are present, with a peak around 23 Hz, which probably corresponds to the resonance frequency of the AQG structure. Around 240 Hz, another weaker resonance seems to occur, but the reasons for it are unknown. At frequencies higher than 300 Hz, electronic noise dominates, making

the signal useless. The sharp peaks seen in the ASD are resonant frequencies, indicating that the ground or nearby structures are more sensitive to these specific vibration frequencies. These resonances can arise from geological features, subsurface structures, or the presence of man-made structures interacting with ground vibrations.

When comparing signals, it is crucial to consider the difference between day and night measurements, as human activities significantly impact ground vibrations. Figure 3.13 illustrates the comparison between time series obtained during the day and during the night.

(a) AQG with compensation and correction   (b) Titan

Figure 3.13.   Comparison of time series between night and day measurement. Day: 15/03/2023 and night: 20/03/2023 both in PML Liège.

As shown in Figure 3.13, vibration levels are significantly lower at night. It is due to human activities which increase vibrations during the day. So, even with vibration compensation, the amplitude of vibrations is important as they cannot be fully compensated for. It demonstrates that vibrations are unavoidable and the quieter the location, the better the precision.

A night measurement enables better visibility of the typical vibrations from the environment without the pollution of human activities. It is clearly visible in Figure 3.14 which represents the ASD of the night and day measurements with Titan.
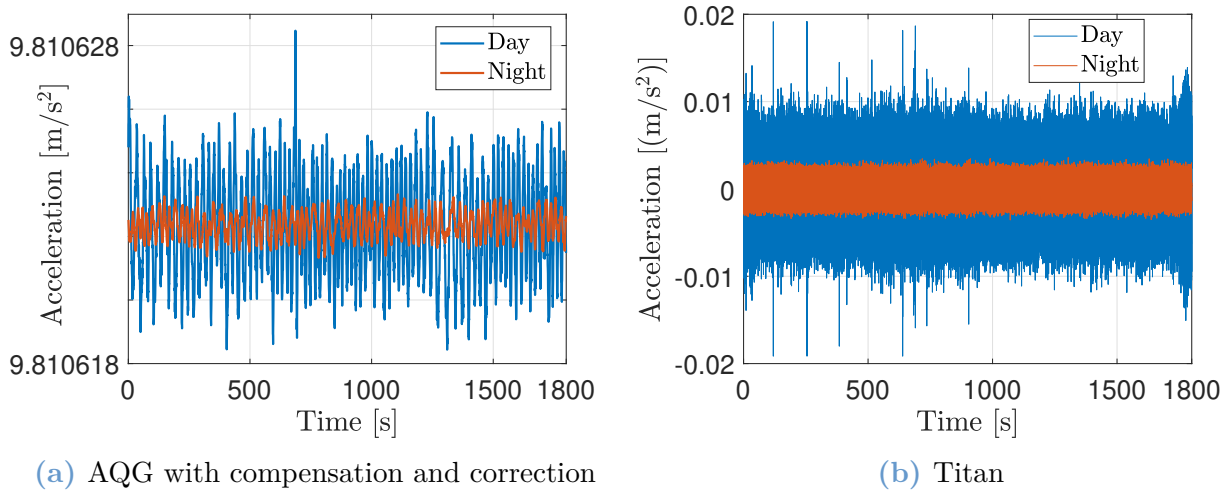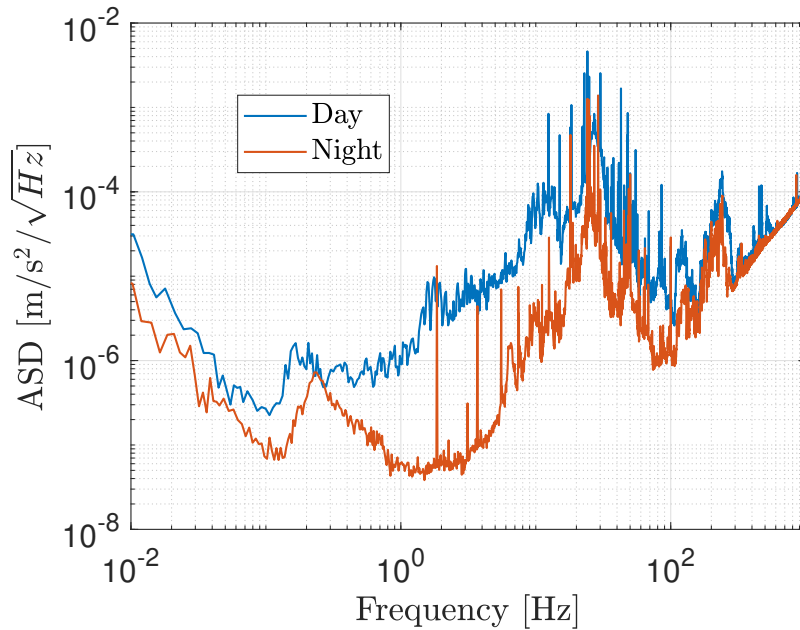
Figure 3.14. Comparison of Titan ASDs between night and day measurement. Day: 15/03/2023 and night: 20/03/2023 both in PML Liège.

The ASD of the night measurement is very similar to that of the April 2 measurement shown in Figure 3.12b. Their behavior is the same except at 240 Hz, the potential resonance is stronger here, perhaps due to a meteorological phenomenon that caused the building to vibrate. The day measurement has a much higher magnitude for frequencies up to 300 Hz beyond which the electronic noise level is the same for night and day measurements, as it is the same sensor. During the day, ground vibrations measured are mainly due to human activities and thus remarkable behavior such as the microseismic peak or the resonance peaks in the range of 1-10 Hz are less or even not visible. The main remaining characteristics are the resonances around 23 Hz likely due to the AQG and the potential resonance at 240 Hz. At very low frequencies, the drift seems stronger too during the day.

Now that the signals gathered by the AQG without compensation and by the Titan are analyzed independently, it is possible to find the link between them. Computing the transfer function is the best way to see the relationship between two sensors. But one of the challenges in this process was to find matching time stamps between the AQG samples and the Titan samples to calculate the transfer function. The time stamps were not aligned during the recordings through the acquisition board, therefore, an algorithm was implemented to address the issue.

Three methods have been tested to determine the transfer function between the AQG signal and the Titan signal, as the relationship between vibrations and output acceleration is not straightforward. The first method involves taking the Titan sample corresponding to the start of the AQG's detection process. The second method involves averaging the vibrations measured by Titan over the interferometer duration. The third method entails weighting the accelerations by the sensitivity function $f(t)$ and then calculating the mean. After processing

the Titan data depending on the method, the transfer function is computed. The results of the three methods are illustrated in Figure 3.15.

(a) One sample

(b) Mean over $2T$

(c) Mean over $2T$ of weighted accelerations by $f(t)$
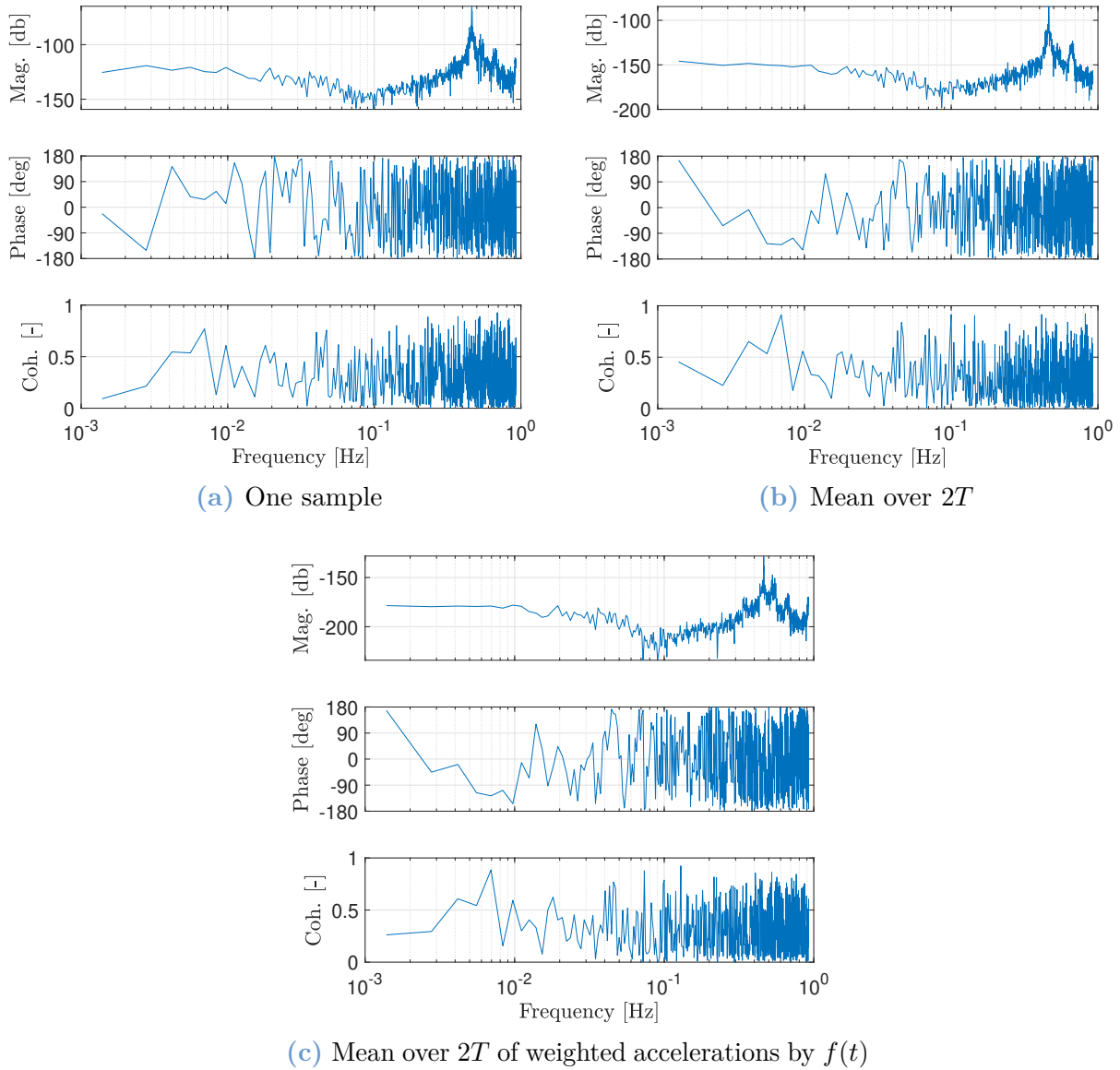
Figure 3.15. Comparison of the transfer functions $\ddot{x}_{\text{Titan}}/\ddot{x}_{\text{AQG}}$ obtained using three methods. 02/04/2023 at night in PML Liège.

Unfortunately, none of the methods provided satisfactory results as the coherence between the two signals was consistently poor. No meaningful relationship could be deduced between them, indicating that they behave independently. A peak is visible at the frequency $f = 0.43$ Hz, corresponding to the drops from the AQG servo-loop which can be seen in the PSD of g_{res} in Figure 3.2. The one-sample method was expected to yield unsatisfactory results, as there is no real correlation between a single measurement and the vibrations impacting the interferometer over 120 ms. The simple mean could have led to meaningful results as it takes into account vibrations over the entire interferometry. However, the effect of the sensitivity

function has been discussed in Section 2.4 and it shows that vibrations do not affect the measurement in the same way throughout the interferometry. Thus the weighting function method with the sensitivity function was tested because it links the interferometric phase and vibration accelerations through Equation 2.13, potentially providing a link between gravity and vibrations. Unfortunately, it was not the case as can be seen in Figure 3.15c.

These findings suggest that the AQG cannot be accurately characterized as a simple accelerometer at low frequencies without vibration compensation. This discrepancy may be attributed to the influence of the sensitivity function on its measurements, as well as to the low sampling frequency and resulting aliasing of high-frequency vibrations. As a result, vibrations have a nonlinear behavior in the AQG measurement, as the high-frequency vibrations affect the low frequencies.

Although exploring phase-based approaches was beyond the scope of this work, it could potentially lead to a meaningful transfer function.

Validation of Titan

To validate the measurements obtained from Titan and ensure that they are not the source of the problem in the transfer functions previously found, an experiment was conducted using two Güralp 6T seismometers from Güralp Systems Limited [38]. An additional purpose of the experiment was to understand how ground vibrations propagate from the ground to the top of the AQG, where the mirror is located.

The experimental setup involved placing one Güralp seismometer on the ground close to the AQG and another on top of the AQG near the reflective mirror and Titan, as shown in Figure 3.16.
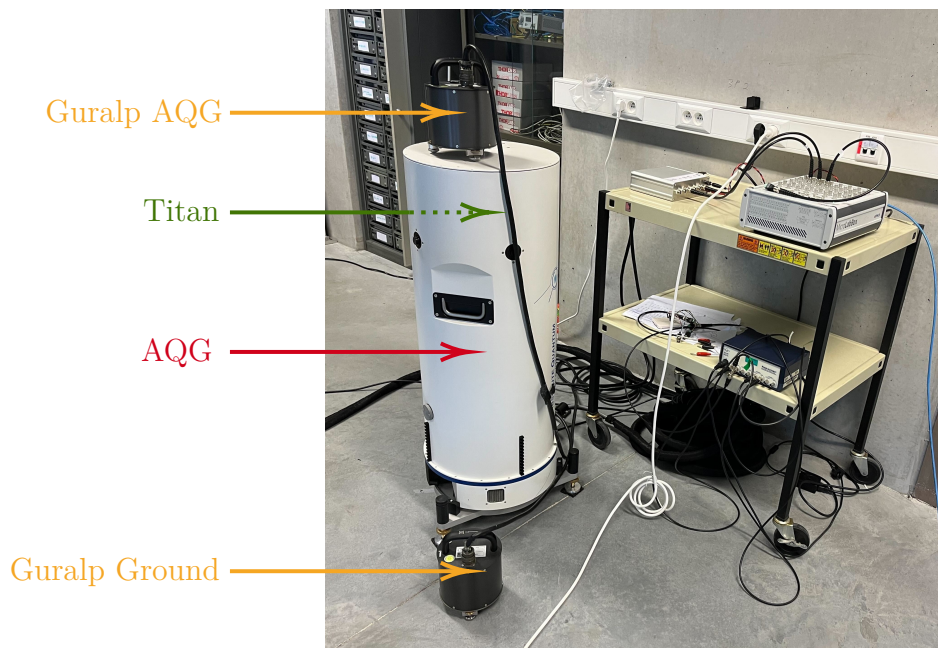

Figure 3.16. Experimental setup.

The Güralp on the ground measured ground vibrations directly, while the one on top of the AQG measured vibrations at the top. The Güralps' signals were recorded in velocity [m/s] since the Güralps are seismometers. An external recorder (National Instrument PXIe) was used with a sampling frequency of $f_s = 50$ kHz for the Güralps, while the Titan was recorded via the acquisition board of the AQG. As the Titan and the Güralps were recorded independently of each other, the time delay between the two had to be computed in post-processing. The starting times from Titan and from the Güralps, accurate to the millisecond level, were used to calculate the delay between the sensors and then align them on the same starting time stamp. Some manual tuning was necessary, as the delay was computed based on information provided by Exail which were approximations and as the given starting times were not precise enough (1 ms = 50 samples at 50 kHz). To have a meaningful comparison, the Güralps' signals were converted to m/s² in post-processing to match the acceleration unit of Titan, which was used in the previous analysis.

Once the data were processed, the ASDs of the three sensors were compared, as shown in Figure 3.17.
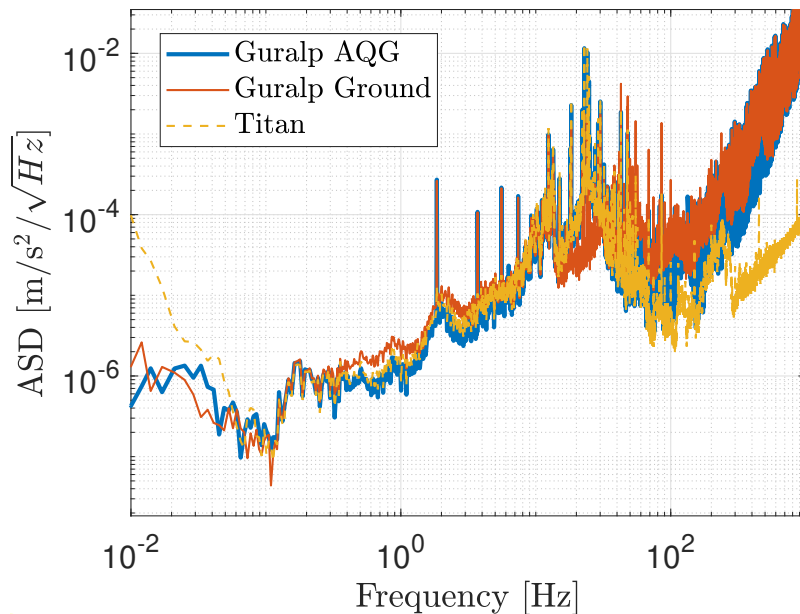
Figure 3.17. Comparison of ASDs from the Güralp on the AQG, the Güralp on the ground, and the Titan. 28/03/2023 in PML Liège.

The three ASDs exhibit similar characteristics, which is a positive outcome. The Titan ASD is slightly higher than the one of the Güralp on the AQG. The difference is due to the fact that the Güralp on the AQG is not exactly at the same position as Titan as it lies on a lid on top of it. Below 0.1 Hz, the three ASDs are no longer superimposed, as the two Güralps are no longer coherent and the Titan has the high-pass filter at 0.05 Hz too. The resonance frequencies below 20 Hz were the same for the Güralp on the AQG and the Güralp on the ground, which is surprising given that the two sensors were located in different places. These frequencies are probably due to the internal structure of the seismometers. The Titan and the Güralp on the AQG exhibit the same resonance peak at 23 Hz, most probably due to the

structure of the AQG, and similar resonance peaks beyond. In contrast, the Güralp on the ground does not exhibit this very high resonance at 23 Hz but still presents similar isolated resonance frequencies as the others. Furthermore, above 23 Hz, the sensors on the AQG tend to feel damped ground vibrations as the Güralp on the ground has a higher amplitude than theirs. It is probably a low-pass filter effect from the device structure. At frequencies higher than 100 Hz, electronic noise dominates both the Güralps, and the Titan signal gets noisy above 300 Hz.

Based on these measurements, transfer functions between each pair of sensors are derived to gain further insights into the transmissibility of vibrations between the ground and the top of the AQG. The transfer functions are shown in Figure 3.18.
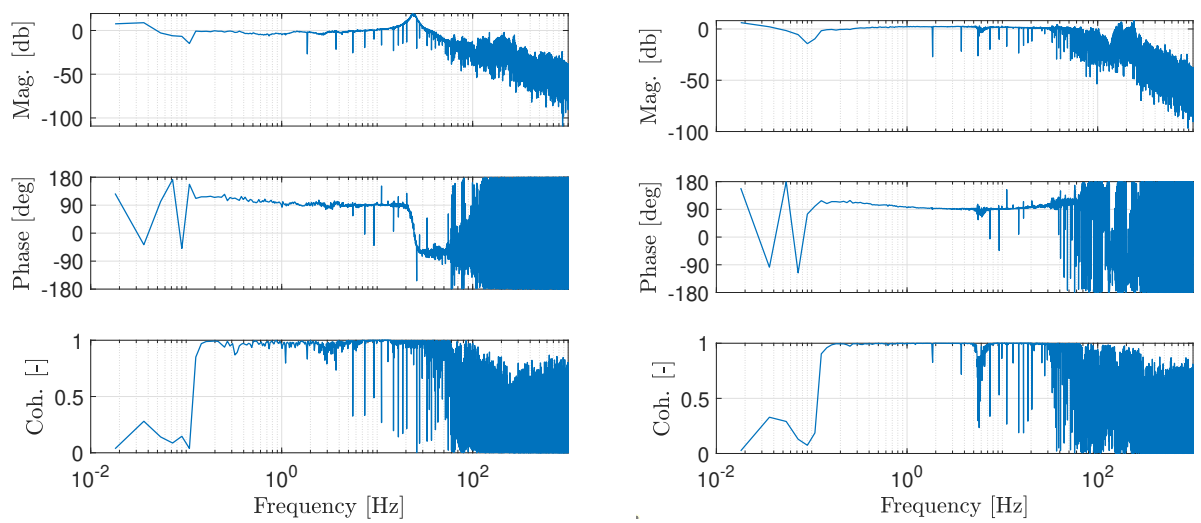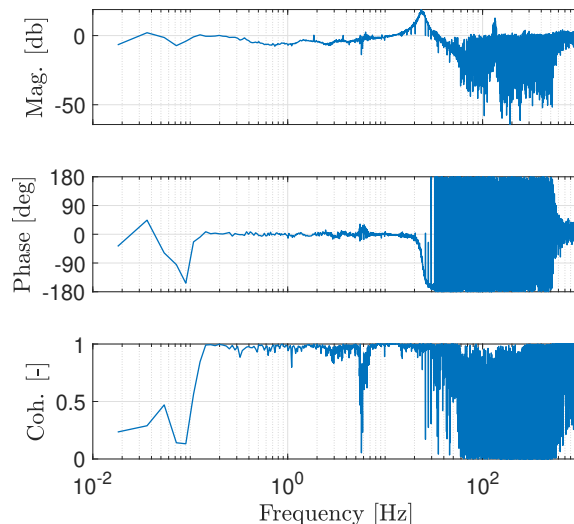

(a) Transfer function $\ddot{x}_\text{Titan}/\ddot{x}_\text{Guralp ground}$

(b) Transfer function $\ddot{x}_\text{Titan}/\ddot{x}_\text{Guralp AQG}$

(c) Transfer function $\ddot{x}_\text{Guralp AQG}/\ddot{x}_\text{Guralp ground}$

Figure 3.18. Transfer functions between each pair of sensors. 28/03/2023 in PML Liège.

The transfer functions provide additional information on vibration transmission between the sensors. The assumed resonance peak of the AQG at 23 Hz is clearly observed in the transfer functions between a sensor on the ground and one on top of the AQG, see Figures 3.18a and 3.18c. A drop in coherence is observed at 5.5 Hz in the three transfer functions indicating a decrease in the correlation between the sensor measurements at that frequency. The reason behind this drop is not known but it could be some coupling effect or cabling being stretched. Still, it is not a problem as the amplitude and the phase show only very slight variations during this coherence drop. However, in Figures 3.18a and 3.18b, this drop is less visible as multiple small drops are present in the coherence above 5.5 Hz as well. These are due to the presence of resonance peaks in both Güralps signals, but which are not visible in the Titan signal. They cause the Güralps and the Titan to not be coherent at such frequencies.

The phase response exhibits a noticeable shift of $-180°$ at 23 Hz, followed by noise in Figures 3.18a and 3.18c. The shift shows that the sensors on top of the AQG feel the vibrations in advance of the ground, once resonance has passed. When looking at the magnitude, there is clearly a low pass filter effect between the ground and the top of the AQG. The phase shift of $-180°$ at 23 Hz indicates that the structure of the AQG acts as a second-order low-pass filter with a cutoff frequency at 23 Hz. In the transfer functions involving Titan, the phase difference between Titan and the Güralps was found to be $90°$ for frequencies below 23 Hz, indicating that Titan lags behind the Güralps in terms of phase (and thus in terms of time) at low frequency.

The transfer functions between Titan and Güralps exhibit drops in their response due to resonance peaks present in the Güralps signal and not in the Titan one. Ground vibrations were transmitted normally until the resonance at 23 Hz, where amplification occurred, followed by electronic noise. Below 0.1 Hz, a loss of coherence was observed in all three transfer functions. This effect is due to the Güralps since, on one hand, their sensitivity decreases at low frequencies, and on the other hand, it becomes sensitive to other directions.

These findings indicate that the measurements obtained with Titan are likely to be valid, and the issue does not stem from Titan itself. The experiment provided a better understanding of how vibrations are transmitted within the AQG, with a 1:1 ratio observed between Titan's measured vibrations and ground vibrations until the resonance at 23 Hz. However, above 100 Hz, the electronic noise dominated the measurements of both the Güralp seismometers, and above 300 Hz, those of Titan. Since the relevant frequency range for analysis is 0.01-100 Hz, the electronic noise has no significant impact on the results.

In conclusion, it was not possible to establish a direct relationship in terms of acceleration between the Titan and the AQG. This leads to the conclusion that vibrations have a nonlinear behavior in the AQG signal. The proper functioning of Titan has been verified, ruling out calibration or other issues with the device. Furthermore, the experiment demonstrated that the vibrations experienced by the AQG differ from those measured on the ground due to the structure of the device, with the top of the AQG being approximately 45 cm above the ground.

3.4 Post-processing compensation tests

In the previous section, the real-time compensation implemented by Exail was analyzed in terms of acceleration, revealing that a comparison between a raw AQG signal and an accelerometer signal cannot be made by simply examining accelerations.

Continuing the investigation into the vibration compensation, a post-compensation algorithm is implemented. The algorithm is tested to assess whether results can be obtained by taking the filtered acceleration signal from the Titan and subtracting it from the AQG signal. For the post-compensation in acceleration, the three simple methods are tested again: one sample, averaging over $2T$ and averaging after weighting by the sensitivity function.

(a) One sample

(b) Mean over $2T$

(c) Mean over $2T$ of weighted accelerations by $f(t)$
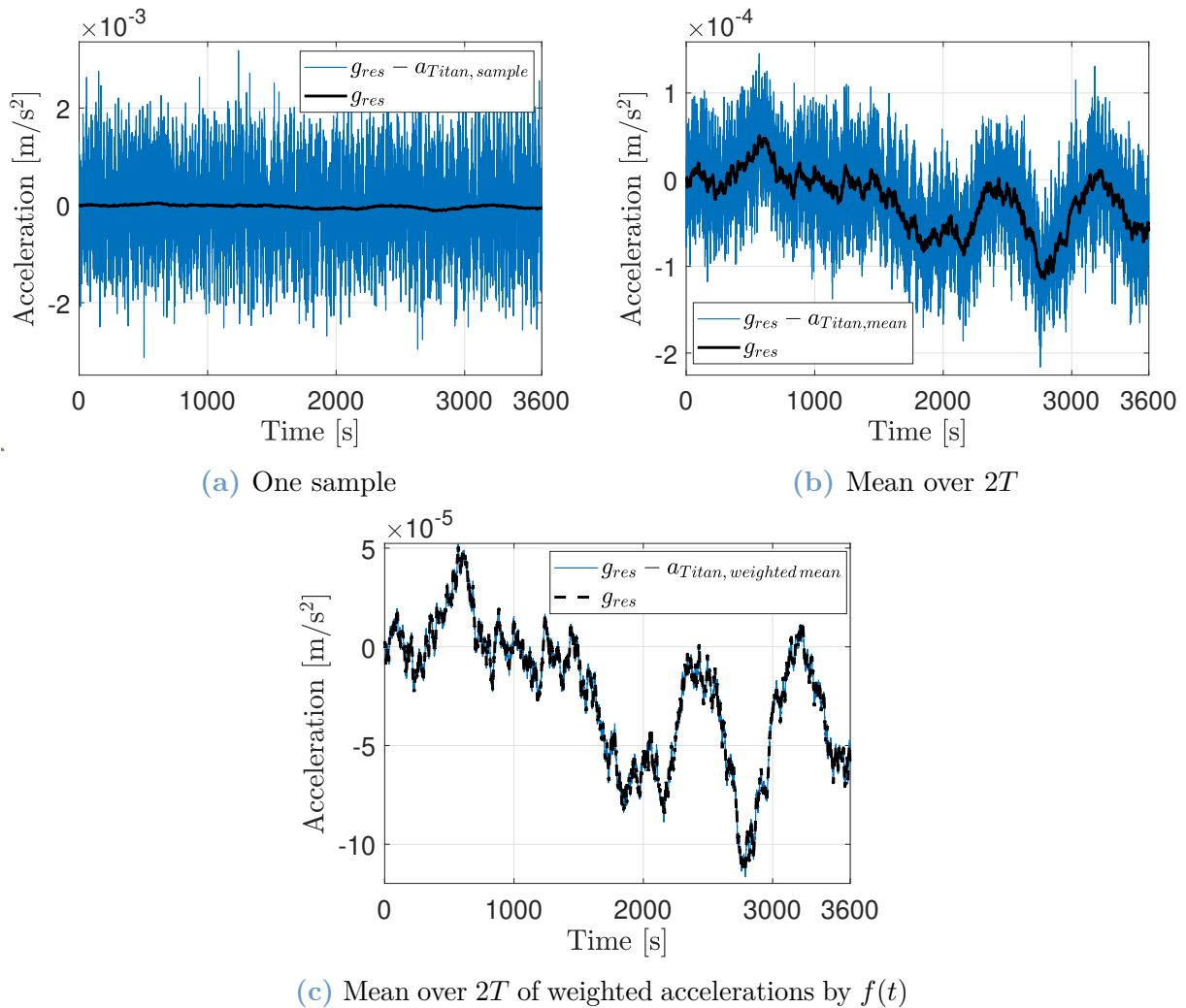
Figure 3.19. Comparison of post-compensation methods. Here, g_{res} is the residual gravity of the non-compensated measurement, so $g_{\text{comp}} - g_{\text{comp},0}$. 02/04/2023 in PML Liège.

These results are unsatisfactory. First, for the methods with one sample and the simple mean, the variations of g are larger with compensation than without. For the weighted mean, no change is observed as the amplitude of the vibrations to be compensated is overly reduced by

the processing. It should compensate vibrations so that g_{res} slightly oscillates around 0, as shown in Figure 3.11a. Thus, the implemented compensation methods either increase the vibrations in the measurement (Figures 3.19a and 3.19b) or have no effect (Figure 3.19c). It can again be attributed to the fact that the working metric is the acceleration. And as with the real-time compensation, the AQG signal cannot be processed or correlated to the vibration signal once it has been converted into accelerations. These results were expected given the poor transfer functions obtained previously between the Titan and the AQG accelerations.

To confirm that acceleration as the working metric is the source of the issue, an attempt is made to implement a post-compensation algorithm in phase, as presented in Section 2.4.2. By revisiting Equation 2.7 and considering that the interferometric phase is nullified by the chirp α, the following equation is obtained:

$$g_{\text{raw}} = \frac{2\pi\alpha T^2}{k_{\text{eff}}T^2} - \frac{\delta\varphi_{\text{laser}}}{k_{\text{eff}}T^2} - \frac{\delta\varphi_{\text{vib}}}{k_{\text{eff}}T^2} \tag{3.5}$$

Since the sensitivity function allows the expression of an acceleration disturbance as a phase disturbance, as shown in Equation 2.13, the acceleration signal from the Titan is converted into phase $\delta\varphi_{\text{vib}}$ and removed from g using the following expression:

$$g_{\text{comp}} = g_{\text{raw}} + \frac{\delta\varphi_{\text{vib}}}{k_{\text{eff}}T^2} \tag{3.6}$$

This approach should compensate for the vibrations. Figure 3.20 displays the result of the used procedure.
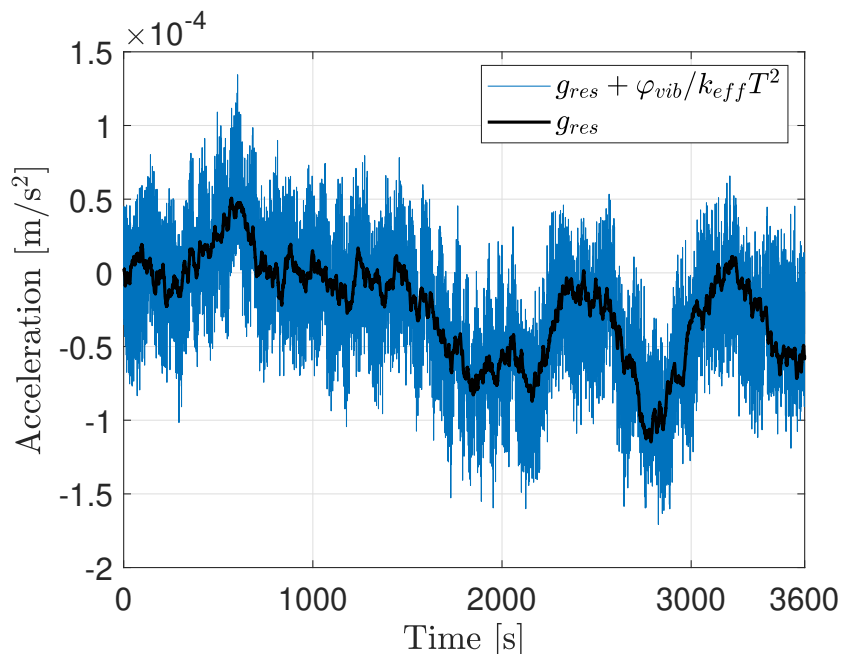

Figure 3.20. Post-compensation of the residual non-compensated gravity working with phases. 02/04/2023 in PML Liège.

As observed in Figure 3.20, compensation does not give concluding results. The post-compensation in phase does not effectively eliminate the vibrations in the measurement as it

increases the variations of g.

The reason for this failure lies in the complexity of the vibration disturbances. Indeed, the vibrations experienced by the AQG exhibit nonlinear behavior due to aliasing, leading to a more intricate relationship between acceleration and phase. Furthermore, as discussed in Section 2.3.2 and 2.4.2, if a vibration produces a difference in the interferometric phase of $\pm\pi$, the interferometric pattern is jammed. Thus, working in post-compensation, this is more than likely that it happens in a noisy environment such as the University.

Additionally, the post-compensation in phase assumes that the vibration disturbances can be accurately measured and directly subtracted from the raw measurement. However, the measurement of vibrations is subject to uncertainties and noise, which introduce errors in the compensation process. Uncertainties, combined with the nonlinear behavior of vibrations, contribute to the inability of the post-compensation in phase to effectively mitigate the vibration effects.

Nor is it impossible for an error in the algorithm to be the cause of an incorrect phase calculation. Further checks should be carried out to ensure that there is no error.

Therefore, despite the intuitive approach of compensating for vibrations by removing the acceleration or the phase disturbances caused by them, post-compensation methods do not yield the desired results. This highlights the challenges involved in accurately compensating for complex vibration disturbances in the measurement of the AQG. Further research and refinement of compensation techniques are necessary to address these challenges and improve the overall performance of the gravimeter.

Chapter 4

Perspectives

This chapter presents the prospects and potential improvements for further enhancing the performance of the AQG based on the conducted studies and findings. To gain a deeper understanding of the techniques and processing used in the AQG in line with the study presented in the previous chapter, it would be crucial to undertake a comprehensive analysis of the signals in phase. This analysis is expected to provide deeper insights into the existing methods and contribute to the advancement of the AQG.

Regarding potential improvements, the first avenue concerns the use of an active isolation platform, as detailed in Section 2.4.1. PML has developed a platform named IGOR, and some experiments were conducted to provide preliminary measurements. The results of these measurements are presented in the subsequent section. Another option is the integration of an accelerometer developed by PML, called µVINS, which possesses characteristics better suited for vibration compensation within the AQG system. Lastly, the implementation of a hybridization approach, combining both the classical accelerometer and the AQG, represents the ultimate goal in terms of performance enhancement. It should be noted that hybridization will be a theoretical review based on existing studies, as other research endeavors have already explored this topic. As PML aims to push the boundaries of AQG performance, it will eventually need to develop its own hybridization algorithm.

4.1 Active vibration isolation with IGOR

IGOR, a six-degree-of-freedom active platform developed by PML [39], serves as an active and passive vibration isolation solution. Its working principle is similar to the one explained in Section 2.4.1, here three laser interferometry-based inertial sensors record the platform's movement, while actuators counterbalance the movement. The platform actively reduces vibrations in the frequency range of 0.1-10 Hz and passively above.

The purpose of using the IGOR platform is to mitigate vibration noise in the AQG. The instrument is placed on the platform, as depicted in Figure 4.1.
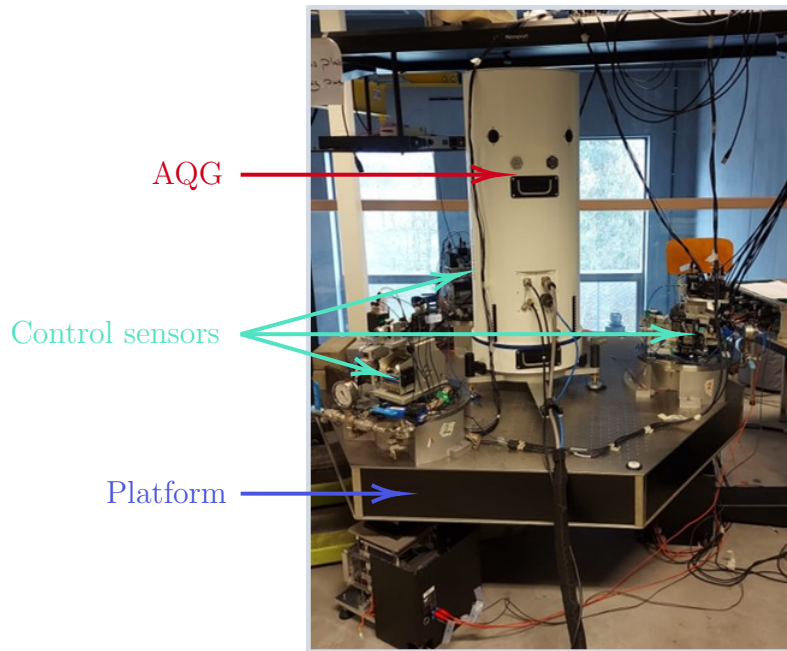
Figure 4.1. AQG mounted on the active platform IGOR.

The obtained results with such a configuration are promising, as the platform effectively attenuates vibration noise, as demonstrated in Figure 4.2.

(a) PSDs

(b) Allan deviations

Figure 4.2. Comparison of PSDs and Allan deviations of the residual compensated gravity with and without the active platform. Measurements taken at PML Liège.

In the PSD, it is evident that the measured signal with the control activated during the night of April 21 exhibits a smaller amplitude compared to when the AQG is on the platform but the control is turned off for the same night (albeit at different times, as simultaneous recording was not possible). When the control is turned off, it implies that the platform does not use any active control, but the passive isolation stage remains effective. Although some

resonances are visible in the signal without control, overall, the vibrations are significantly reduced with the active control, demonstrating its beneficial effect.

The impact of active compensation can be observed in Figure 4.3, which represents the PSD of accelerations measured by one of the control sensors on the platform with and without control. As anticipated, the vibrations are well attenuated by approximately one order of magnitude in the frequency range of 0.1-10 Hz.
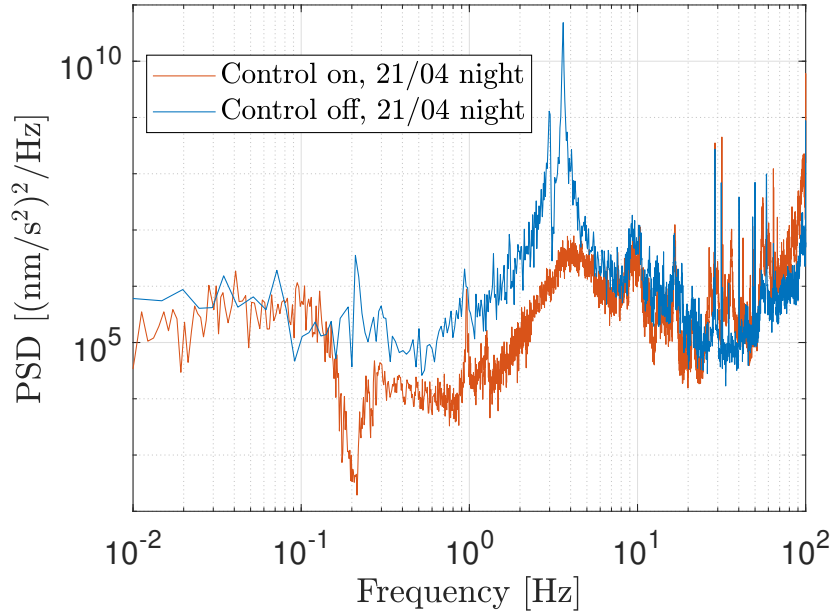
Figure 4.3. PSD of a control sensor on the IGOR platform, with and without active control.

With the control activated, the white noise plateau in the PSD in Figure 4.2a falls even below the best measurement obtained with the AQG on the ground during the Easter vacation on April 15. This remarkable result is further confirmed by examining the Allan deviation of the different signals in Figure 4.2b, where the measurement with the control activated achieves a sensitivity equal to the self-noise of the AQG ($350 \ \mathrm{nm}/s^2/\sqrt{\mathrm{Hz}}$). Indeed, the white noise region follows a slope of $-1/2$ in the log-log plot, and the value of the slope at $\tau = 1$ s gives the sensitivity of the instrument. In this case, it is equal to $350 \ \mathrm{nm}/s^2$.

However, it is essential to be cautious about these results, as subsequent tests exhibited poorer performances. Additional measurements were taken to assess the repeatability of the achieved results, but the AQG did not reach its self-noise limit again. Figure 4.4 compares the different results.
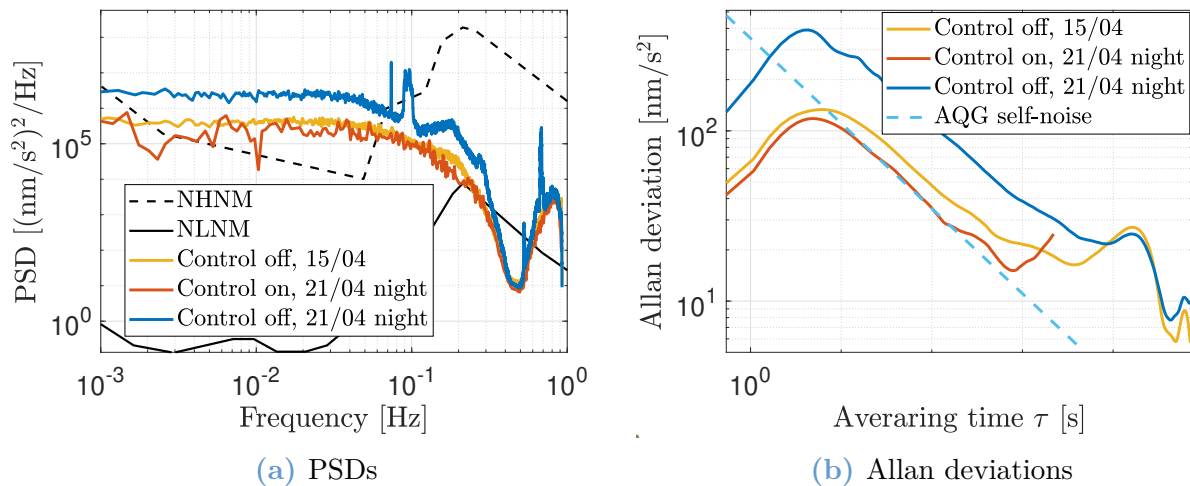
(a) PSDs
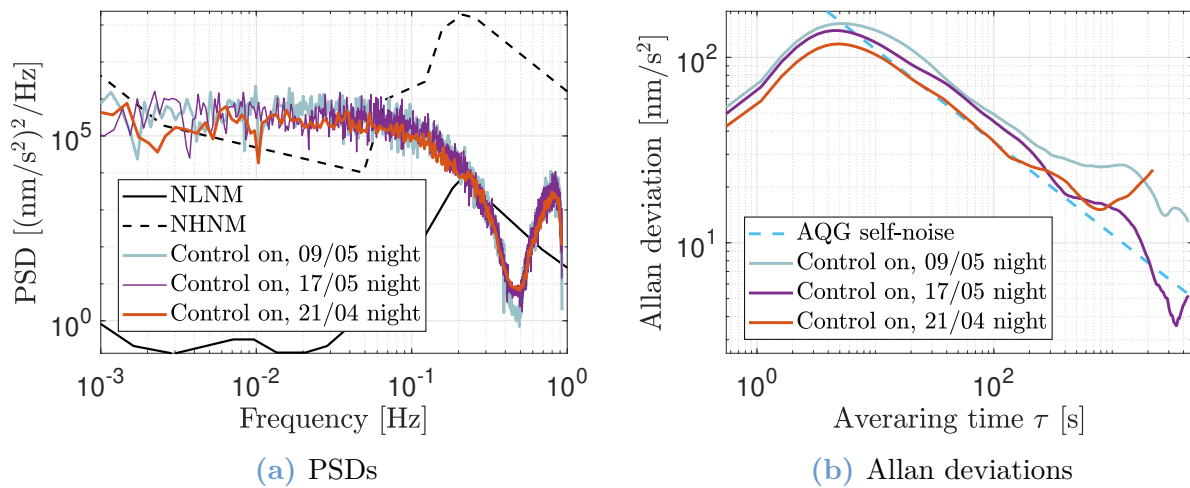
(b) Allan deviations

Figure 4.4. Comparison of PSDs and Allan deviations of the residual compensated gravity with the active platform. Measurements taken at PML Liège.

The measurements from May 9 and May 17 exhibit worse sensitivity, as indicated by their higher Allan deviations compared to the April 21 measurement. While the difference is less apparent in the PSD plot, the PSD of April 21 is still slightly below the others on the white noise plateau. It should be noted that in each case, the resonance frequencies are successfully suppressed, which is already a significant achievement. An interesting feature in the Allan deviation of the May 17 measurement is visible, where the curve dips below the AQG self-noise, which is theoretically impossible. This observation suggests a potentially incorrect approximation of the AQG self-noise or a problem linked to the computation of the Allan deviation.

To ensure comparability, the PSDs of the control sensors also need to be analyzed. Figure 4.5 illustrates the PSD of a control sensor in the three different measurement scenarios.

Figure 4.5. PSD of a control sensor on the IGOR platform for different measurements.

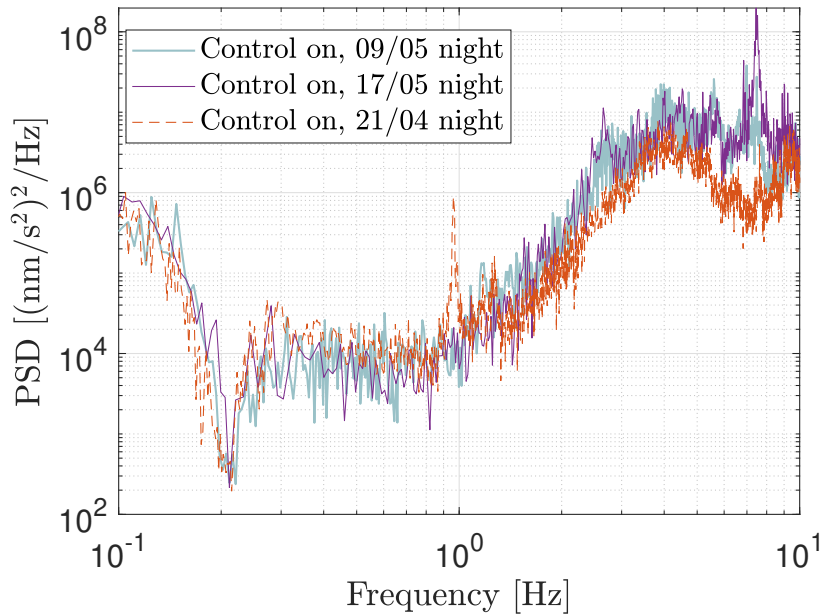These curves align with the obtained results, as the vibrations sensed by the control sensors on April 21 are lower than in the other two cases. The two other curves also exhibit a peak around 7.5 Hz, whereas the orange curve demonstrates a decrease at this frequency. It shows that weaker vibrations reached the top of the platform during the measurement on April 21.

The poorer results obtained after the initial measurement can be attributed to various factors, such as geological, meteorological, or other external influences. In particular, it is known that it rained heavily during the night of May 9, leading to gravity variations due to the added mass and induced ground vibrations. Further investigation is required to fully comprehend the obtained results and ensure their repeatability. Nevertheless, active vibration isolation presents a promising direction for reducing vibration noise and enhancing the performance of the AQG. In fact, the self-noise limit has never been reached before with an AQG of Exail. It opens the door to new improvements touching the laser phase noise.

4.2 The accelerometer µVINS

An alternative approach to improve vibration compensation involves the use of a sensor developed by PML, which demonstrates more suitable performance for this purpose compared to Titan. The sensor is called the µVINS, a compact and highly precise interferometric inertial sensor [40]. Figure 4.6 illustrates the µVINS sensor.
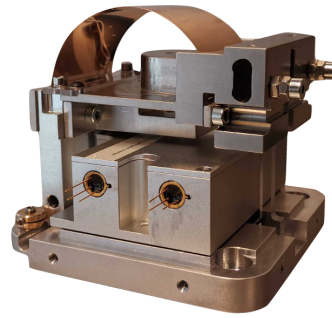
Figure 4.6. µVINS sensor

Replacing Titan with the µVINS sensor in the AQG holds the potential to significantly enhance vibration compensation. There are two primary advantages associated with the µVINS sensor. Firstly, it exhibits lower self-noise. Secondly, µVINS should require fewer filters, as it is specially designed to have a flat phase in the frequency range of interest.

A comparison between the self-noise of µVINS and Titan is presented in Figure 4.7.
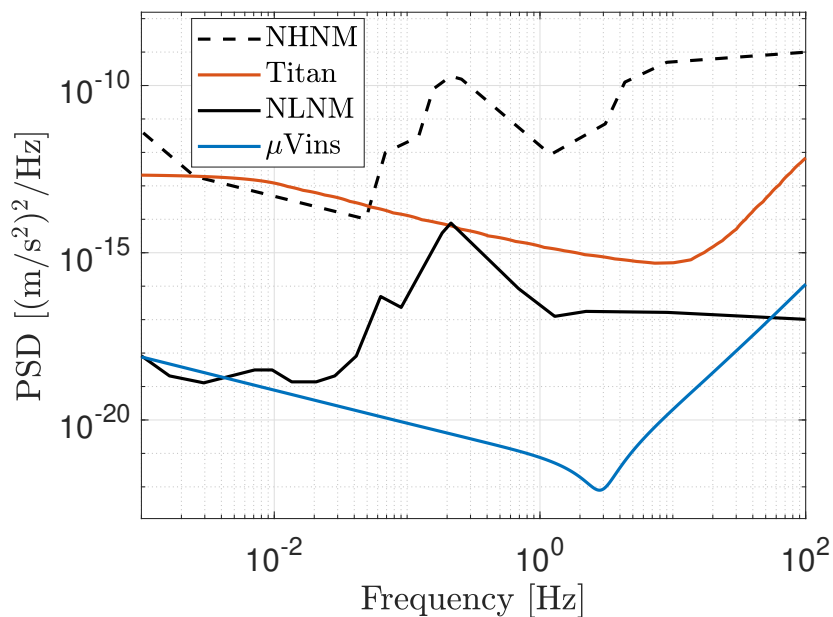
Figure 4.7. Comparison of the PSD self-noise between Titan and µVins.

The self-noise of the µVINS sensor remains below the NLNM curve and, consequently, is lower than that of Titan. This characteristic ensures that the µVINS sensor does not impose any limitations on the measurement of seismic vibrations within the range of interest 0.01-100 Hz. Consequently, it becomes feasible to measure very small vibrations without interference from µVINS self-noise.

Initial tests have been conducted on the AQG, using the µVINS sensor as a replacement for Titan. All electronic and acquisition components have remained unchanged, with only the

sensor being substituted to assess its behavior. Figure 4.8 illustrates the integration of µVINS within the AQG setup.
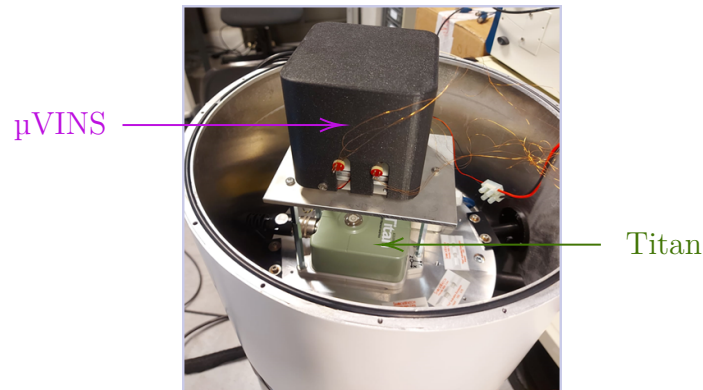
Figure 4.8. Integration of µVINS in the AQG.

Preliminary results of the real-time compensation, incorporating the µVINS sensor instead of Titan and keeping the acquisition chain of Exail, have not yet yielded conclusive findings. Further research and experimentation are necessary to fully evaluate the performance of the µVINS sensor. Moreover, such an evaluation would likely involve modifying the existing acquisition chain implemented by Exail for Titan to adapt it to the µVINS sensor. This operation is delicate, as it requires accessing the internal electronics of the instrument.

4.3 Hybridization

Another idea for enhancing the performance of the AQG involves hybridization, which combines the AQG with an accelerometer. This configuration allows for the incorporation of the strengths of both sensors.

The AQG exhibits ultra-high sensitivity and excellent long-term stability but is limited by a small bandwidth and dead times during which no measurements are taken. Mechanical accelerometers, on the other hand, possess wide bandwidths and high dynamic ranges but are prone to long-term bias and scale factor drifts. By hybridizing the two sensors, it becomes possible to create a high-bandwidth, high-dynamic range, and ultra-stable accelerometer.

The concept behind hybridization is depicted in Figure 4.9.
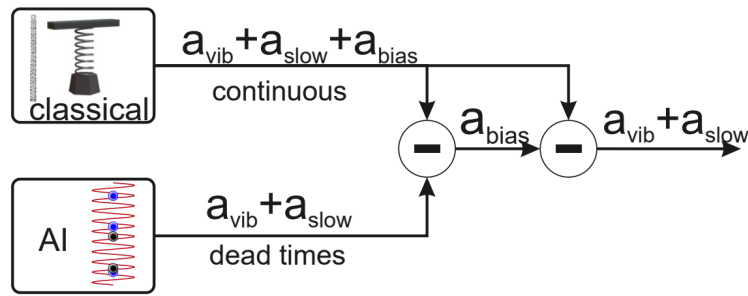
Figure 4.9. Hybridization strategy. a_{vib} is the vibrations accelerations, a_{slow} is the gravitational acceleration and a_{bias} is the bias drift of the acceleration. Figure from [22]

Essentially, by using the drift-free signal from the AQG, it becomes possible to eliminate the bias drift of the accelerometer. As a result, the hybrid sensor's short-term sensitivity is determined by the classical accelerometer noise, while its long-term stability is provided by the AQG.

However, the hybridization process is not straightforward, as previously observed in Chapter 3, the vibrations affect the AQG in a nonlinear way. Different studies have explored various algorithms for combining the two sensors. For example, J. Lautier *et al.* [23] developed a hybrid sensor that links the DC component of the accelerometer to the measured gravity changes by the atom gravimeter. P. Cheiney *et al.* [2, 22] and Z. Zhuoyang *et al.* [41] proposed a fusion algorithm based on a Kalman filter. Additionally, X. Wang *et al.* [29] introduced a maximum likelihood probabilistic data fusion method.

Further researches in this field hold promise for enabling the use of cold-atom gravimeters in inertial navigation applications and in noisy environments in general.

Chapter 5

Conclusion

In conclusion, this thesis has focused on analyzing and improving the performance of the AQG, with a specific emphasis on vibration compensation techniques. An in-depth examination of the working principle and limitations of the AQG, as well as the impact of vibrations on its performance, has yielded important insights.

The analysis revealed that the AQG is subject to three main sources of noise: detection noise, laser phase noise, and vibration noise. Among these, vibration noise was identified as the most limiting factor, even with vibration compensation techniques. Therefore, the search for improvement primarily focused on addressing vibration-induced noise.

The review of vibration mitigation techniques highlighted the effectiveness of vibration compensation through the use of an additional inertial sensor. This approach involves measuring vibrations and then compensating for them in real-time within the AQG. It was found to be more portable and robust than other techniques such as active or passive isolation platforms.

Further investigation into the vibration compensation technique using the accelerometer Titan demonstrated its potential in reducing vibration-induced noise. However, the complex measurement principle of the AQG, as well as the nonlinear behavior of vibrations within the system, posed challenges in establishing a direct correlation between the raw AQG gravity signal and the acceleration measured by Titan.

Attempts at post-processing compensation algorithms were inconclusive, partly due to the complex nature of vibrations in the AQG. The low sampling frequency of the AQG led to aliasing and thus nonlinear behavior, making it difficult to effectively compensate for high-frequency vibrations.

Nevertheless, this research identified potential avenues for improving AQG performance. The use of an active isolation platform, such as the IGOR developed by PML, showed promising results in further reducing vibration noise. By employing the active platform, vibration levels were reduced below the AQG's self-noise, leading to a sensitivity of 350 $\mathrm{nm/s^2}/\sqrt{\mathrm{Hz}}$, a previously unattained performance for Exail's AQG.

The exploration of the µVINS accelerometer developed by PML, specifically designed for AQG vibration compensation, also holds promises for performance enhancement. The µVINS low

self-noise and reduced need for filtering make it an attractive alternative to Titan. Although preliminary results are not yet conclusive, further research and testing are required to fully understand its capabilities.

Additionally, the concept of hybridization between the AQG and a classical accelerometer presents an intriguing possibility. By combining the stability of the AQG with the wide bandwidth of a classical accelerometer, it is possible to create a high dynamic range and ultra-stable accelerometer. Although this concept remains theoretical for the moment at PML, it has already been proven to work in other studies. It, therefore, represents a promising avenue for future research and development at PML.

Overall, this thesis has contributed to the understanding of AQG performance characteristics, limitations, and vibration compensation techniques. The findings provide a foundation for further research and advancements in AQG technology. By addressing the challenges posed by vibration noise and exploring potential improvements, this work paves the way for future advancements in gravimetry applications across various scientific and industrial fields.

In conclusion, this research has provided valuable insights into the performance of the AQG and potential avenues for improvement. The knowledge gained from this study serves as a stepping stone for further investigations and developments in the field of gravimetry. It is our hope that the findings presented here will contribute to the advancement of precise and accurate gravity measurements, enabling new discoveries and applications in diverse fields.

Bibliography

[1] B. Fang *et al.*, "Metrology with Atom Interferometry: Inertial Sensors from Laboratory to Field Applications," *Journal of Physics: Conference Series*, vol. 723, no. 1, Jun. 2016, 012049. DOI: 10.1088/1742-6596/723/1/012049.

[2] P. Cheiney *et al.*, "Navigation-Compatible Hybrid Quantum Accelerometer Using a Kalman Filter," *Physical Review Applied*, vol. 10, no. 3, Sep. 2018, 034030. DOI: 10.1103/PhysRevApplied.10.034030.

[3] Y. Bidel *et al.*, "Absolute marine gravimetry with matter-wave interferometry," *Nature Communications*, vol. 9, no. 1, Feb. 2018, 627. DOI: 10.1038/s41467-018-03040-2.

[4] A. Jageler, "Improved Hydrocarbon Reservoir Evaluation Through Use of Borehole-Gravimeter Data," *Journal of Petroleum Technology*, vol. 28, no. 06, pp. 709–718, Jun. 1976. DOI: 10.2118/5511-PA.

[5] P. Vajda, "Recent Developments and Trends in Volcano Gravimetry," in *Updates in Volcanology*, K. Nemeth, Ed., Rijeka: IntechOpen, 2016, ch. 4. DOI: 10.5772/63420.

[6] C. Freier *et al.*, "Mobile quantum gravity sensor with unprecedented stability," *Journal of Physics: Conference Series*, vol. 723, no. 1, Jun. 2016, 012050. DOI: 10.1088/1742-6596/723/1/012050.

[7] A.-K. Cooke, C. Champollion, and N. Le Moigne, "First evaluation of an absolute quantum gravimeter (AQG#B01) for future field experiments," *Geoscientific Instrumentation, Methods and Data Systems*, vol. 10, no. 1, pp. 65–79, Mar. 2021. DOI: 10.5194/gi-10-65-2021.

[8] V. Ménoret *et al.*, "Gravity measurements below 10^{-9} g with a transportable absolute quantum gravimeter," *Scientific Reports*, vol. 8, no. 1, Aug. 2018, 12300. DOI: 10.1038/s41598-018-30608-1.

[9] A. Peters, K. Y. Chung, and S. Chu, "High-precision gravity measurements using atom interferometry," *Metrologia*, vol. 38, no. 1, Feb. 2001, 25. DOI: 10.1088/0026-1394/38/1/4.

[10] W. Gong, A. Li, C. Huang, H. Che, C. Feng, and F. Qin, "Effects and Prospects of the Vibration Isolation Methods for an Atomic Interference Gravimeter," *Sensors*, vol. 22, no. 2, Jan. 2022, 583. DOI: 10.3390/s22020583.

[11] X. Wu *et al.*, "Gravity surveys using a mobile atom interferometer," *Science Advances*, vol. 5, no. 9, Sep. 2019, eaax0800. DOI: 10.1126/sciadv.aax0800.

[12] M.-K. Zhou *et al.*, "Performance of a cold-atom gravimeter with an active vibration isolator," *Physical Review Applied*, vol. 86, no. 4, Oct. 2012, 043630. DOI: `10.1103/PhysRevA.86.043630`.

[13] F. Yver-Leduc *et al.*, "Reaching the quantum noise limit in a high-sensitivity cold-atom inertial sensor," *Journal of Optics B: Quantum and Semiclassical Optics*, vol. 5, no. 2, Apr. 2003, S136. DOI: `10.1088/1464-4266/5/2/371`.

[14] L. L. Richardson, " Inertial noise post-correction in atom interferometers measuring the local gravitational acceleration," Ph.D Dissertation, Hannover : Gottfried Wilhelm Leibniz Universität, 2019. DOI: `http://dx.doi.org/10.15488/4434`.

[15] J. Le Gouët *et al.*, "Limits to the sensitivity of a low noise compact atomic gravimeter," *Applied Physics B*, vol. 92, no. 2, pp. 133–144, Aug. 2008. DOI: `10.1007/s00340-008-3088-1`.

[16] Joint Research Centre (European Commission) and M. Travagnin, *Cold atom interferometry sensors : physics and technologies : a scientific background for EU policymaking.* Publications Office, 2020. DOI: `10.2760/315209`.

[17] µQuans, *Absolute Quantum Gravimeter : A free-fall absolute gravimeter based on laser-cooled atoms*, datasheet, 2019. [Online]. Available: `https://www.muquans.com/wp-content/uploads/2019/03/muquans_aqg.pdf`.

[18] F. Pereira dos Santos and S. Bonvalot, "Cold-Atom Absolute Gravimetry," in *Encyclopedia of Geodesy*, E. Grafarend, Ed. Cham: Springer International Publishing, Jul. 2016, pp. 1–6. DOI: `10.1007/978-3-319-02370-0_30-2`.

[19] R. Geiger, A. Landragin, S. Merlet, and F. Pereira Dos Santos, "High-accuracy inertial measurements with cold-atom sensors," *AVS Quantum Science*, vol. 2, no. 2, Jun. 2020, 024702. DOI: `10.1116/5.0009093`.

[20] µQuans, *Formulaire AQG*.

[21] µQuans, *g measurement using cold atoms*, Mar. 2018.

[22] P. Cheiney *et al.*, "Demonstration of a Robust Hybrid Classical/Quantum Accelerometer," in *2019 IEEE International Symposium on Inertial Sensors and Systems (INERTIAL)*, 2019, pp. 1–4. DOI: `10.1109/ISISS.2019.8739762`.

[23] J. Lautier *et al.*, "Hybridizing matter-wave and classical accelerometers," *Applied Physics Letters*, vol. 105, no. 14, Oct. 2014, 144102. DOI: `10.1063/1.4897358`.

[24] P. Cheinet, "Conception et réalisation d'un gravimètre à atomes froids," Ph.D Dissertation, Université Pierre et Marie Curie - Paris VI, Mar. 2006. [Online]. Available: `https://theses.hal.science/tel-00070861`.

[25] A. Landragin, "Interférométrie atomique : applications aux capteurs inertiels," Ph.D Dissertation, Université Pierre et Marie Curie - Paris VI, Dec. 2009. [Online]. Available: `https://theses.hal.science/tel-00454671`.

[26] R. Geiger, "Atom interferometry: from fundamental physics to precision inertial measurements," Ph.D Dissertation, Sorbonne Université, Jun. 2019. [Online]. Available: `https://theses.hal.science/tel-02267800`.

[27] µQuans, *AQG : fonctionnement simplifié et modèle de sensibilité.*

[28] C. Janvier, V. Ménoret, B. Desruelle, S. Merlet, A. Landragin, and F. Pereira dos Santos, "Compact differential gravimeter at the quantum projection-noise limit," *Physical Review A*, vol. 105, no. 2, Feb. 2022, 022801. DOI: `10.1103/PhysRevA.105.022801`.

[29] X. Wang *et al.*, "Enhancing Inertial Navigation Performance via Fusion of Classical and Quantum Accelerometers," *The Journal of Navigation*, Mar. 2021. arXiv: `2103.09378 [quant-ph]`.

[30] μQuans, *AQG#A04 : User guide*.

[31] μQuans, *Théorie : compensation des vibrations*, Nov. 2021.

[32] μQuans, *Compensation des vibrations*, Sep. 2019.

[33] J. R. Peterson and U.S. Geological Survey, "Observations and modeling of seismic background noise," English, USGS Publications Warehouse, Open-File Report 93-322, 1993. DOI: `10.3133/ofr93322`.

[34] J. Berger, P. Davis, and G. Ekström, "Ambient Earth noise: A survey of the Global Seismographic Network," *Journal of Geophysical Research: Solid Earth*, vol. 109, no. B11, 2004. DOI: `https://doi.org/10.1029/2004JB003408`.

[35] R. K. Cessaro, "Sources of primary and secondary microseisms," *Bulletin of the Seismological Society of America*, vol. 84, no. 1, pp. 142–148, Feb. 1994. DOI: `10.1785/BSSA0840010142`.

[36] Nanometrics, *Titan Accelerometer*, datasheet, [Online]. Available: `https://nanometrics.ca/products/accelerometers/titan` and `https://ds.iris.edu/NRL/sensors/nanometrics/RESP.XX.NS125..BNZ.Titan.DC_430.20V.0_25G`.

[37] V. Ménoret, *Calcul du délai de l'accéléro Titan à partir des DSP*, Nov. 2015.

[38] Güralp Systems Limited, *Güralp 6T : User's Guide*, MAN-T60-0001, Mar. 2018. [Online]. Available: `https://www.guralp.com/products/surface#seismometers`.

[39] J. Watchi *et al.*, "Experimental validation for low frequency isolation of six degree of freedom systems using inertial sensors," ISMA-USD Noise and Vibration Engineering Conference, Leuven, Belgium, 2022.

[40] A. Amorosi, "High resolution compact vertical inertial sensor for atomic quantum gravimeter hybridizing," ERC - European Research Council [BE], Leuven, Belgium, Sep. 2022. [Online]. Available: `https://hdl.handle.net/2268/295204`.

[41] Z. Zhuoyang, W. Bin, H. Tiantian, and S. Kaichen, "A Fusion Algorithm of Underwater Dual-Sensor Gravimeter," *IEEE Sensors Journal*, vol. 22, no. 1, pp. 461–471, 2022. DOI: `10.1109/JSEN.2021.3126379`.

[42] P. Stoica and R. Moses, "Spectral Analysis of Signals," *Pearson Prentice Hall*, Jan. 2005.

[43] D. W. Allan, "Statistics of atomic frequency standards," *Proceedings of the IEEE*, vol. 54, no. 2, pp. 221–230, Feb. 1966. DOI: `10.1109/PROC.1966.4634`.

[44] D. S. Arar. "Introduction to Allan Variance: Non-overlapping and Overlapping Allan Variance," All About Circuits. (Jul. 2022), [Online]. Available: `https://www.allaboutcircuits.com/technical-articles/intro-to-allan-variance-analysis-non-overlapping-and-overlapping-allan-variance/` (visited on 04/19/2023).

[45]   A. Szczęsna *et al.*, "Inertial Motion Capture Costume Design Study," *Sensors*, vol. 17, no. 3, Mar. 2017, 612. DOI: 10.3390/s17030612.

Appendix A

Power Spectral Density

The Power Spectral Density (PSD), denoted as $\gamma_x(f)$, characterizes the distribution of power across the frequency components of a time series signal $x(t)$ [42]. It is computed by applying the Fourier transform to the autocorrelation function $\Gamma_{xx}(\tau)$ of the signal:

$$\gamma_x(f) = \int_{-\infty}^{\infty} \Gamma_{xx}(\tau) e^{-2\pi j f \tau} d\tau$$

$$\Gamma_{xx}(\tau) = \int_{-\infty}^{\infty} x(t) x^*(t - \tau) dt \tag{A.1}$$

The PSD is particularly useful for analyzing vibration signals that have limited information in the time domain. It enables the examination of the frequency content of the signal and the identification of dominant vibration frequencies. Additionally, it provides insights into the noise spectrum, facilitating the application of appropriate filters for noise removal.

In the literature and in this report, Amplitude Spectral Density (ASD) is often used instead of PSD. The ASD is the square root of the PSD and allows for analysis in physical units.

Numerical Implementation

The computation of PSDs was primarily performed using MATLAB. The `pwelch` function in MATLAB was used for this purpose, and it was used as follows: `[pxx, f] = pwelch(x, window, noverlap, nfft, fs)`.

Appendix B

Allan Deviation

The Allan deviation is a statistical analysis tool developed by David W. Allan in 1966 [43]. It quantifies the frequency stability of a signal in the time domain and helps identify noise sources originating from random processes, such as bias drift and quantization noise. Initially used to measure the frequency stability of precision oscillators, the Allan deviation has been extended to various applications, including the study of random processes in inertial sensors like gyroscopes and accelerometers.

The non-overlapping Allan variance, denoted as $\sigma_y^2(\tau)$, is mathematically defined as follows [44]:

$$\sigma_y^2(\tau) = \frac{1}{2(N-1)} \sum_{n=1}^{N-1} (y_{n+1} - y_n)^2 \tag{B.1}$$

where τ is the averaging time and N is the number of groups of length τ in the data set. The Allan deviation is then calculated as $\sigma_y(\tau) = \sqrt{\sigma_y^2(\tau)}$.

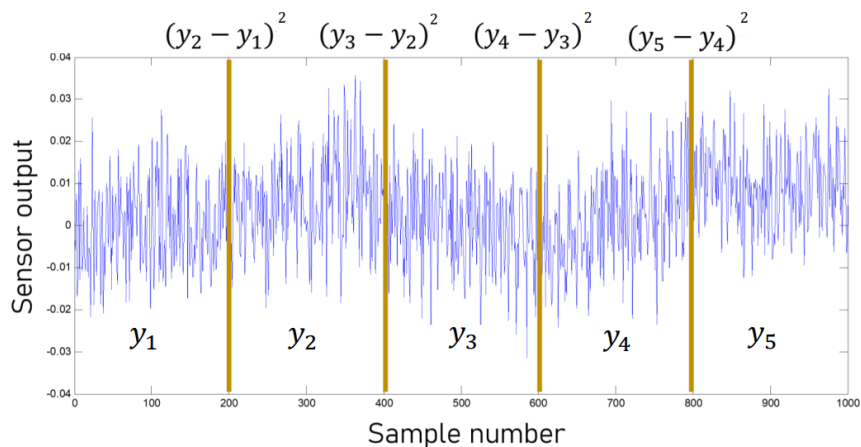To illustrate this concept, consider the following example:

Figure B.1. Example of time series.

The set of samples is partitioned into groups of a certain size, determined by the averaging time τ. The mean y_n within each partition is computed, and the differences

II

between adjacent mean values are evaluated. The Allan variance is then calculated as half the average of the squared differences. For example, taking the time series in Figure B.1:

$$\sigma_y^2(\tau) = \frac{1}{2} \frac{(y_2 - y_1)^2 + (y_3 - y_2)^2 + (y_4 - y_3)^2 + (y_5 - y_4)^2}{4}$$

This process is repeated for different τ values. The minimum possible τ is equal to the size of one sample. In the example, $\tau_{\min} = 0.1$ s. As τ increases, the averaged groups become larger, corresponding to lower frequencies.

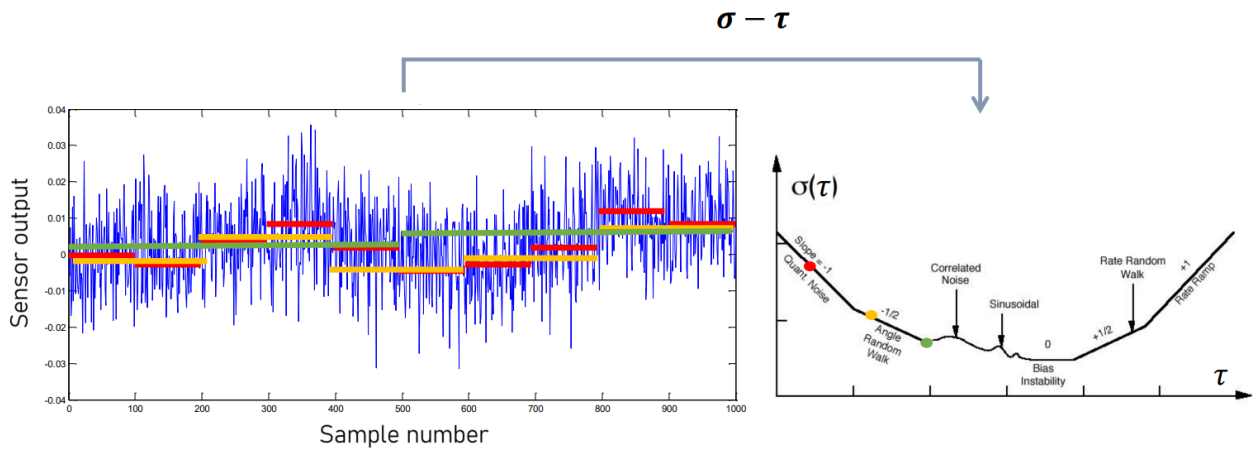The square root of the Allan variance gives the Allan deviation. A typical Allan plot is shown in Figure B.2:

Figure B.2. Example of Allan deviation graph. Adapted figure from [45].

In Figure B.2, different colors represent different averaging times τ. The Allan plot is commonly presented in a log-log scale. It reveals seven distinct noise sources that contribute to the overall drift. These noise sources can also be observed in the power spectral density, but they are more clearly visible and easier to interpret using the Allan deviation. The graph can be interpreted in terms of frequency, with small τ corresponding to high frequencies and large τ corresponding to low frequencies.

The seven noise sources characterized by the Allan deviation are as follows [45] (corresponding to the slopes in the log-log plot):

- Quantization noise with a slope of -1.

- White noise with a slope of $-1/2$.

- Bias instability, which corresponds to the minimum of the curve and has a slope of 0. It is caused by low-frequency random fluctuations in the electronics.

- Rate random walk with a slope of $+1/2$.

- Rate ramp or drift with a slope of $+1$.

Two additional noise sources, which are less prominent, include:

- Correlation noise, indicated by a $+1/2$ slope followed by a $-1/2$ slope.

- Sinusoidal noise, which appears as alternating $+1$ and -1 slopes.

Numerical Implementation

To compute the Allan deviation in MATLAB, the `allanvar` function is used. This function calculates the Allan variance, which needs to be square-rooted to obtain the Allan deviation. The function is used as follows: `[avar, tau] = allanvar(Omega, m, fs)`.